



UNIVERSIDAD DE INVESTIGACIÓN DE TECNOLOGÍA EXPERIMENTAL YACHAY

Escuela de Ciencias Físicas y Nanotecnología

TÍTULO: GREEN SYNTHESIS OF HARD CARBON NANOSTRUCTURES

Trabajo de integración curricular presentado como requisito para
la obtención del título de Ingeniera en Nanotecnología

Autora:

María Daniela Serrano Larrea

Tutor:

Dr. Julio Chacón Torres

Co-Tutor:

M.Sc. José Luis Flores de la Torre

Urququí, junio de 2024

Autoría

Yo, **MARÍA DANIELA SERRANO LARREA**, con cédula de identidad 0105125058, declaro que las ideas, juicios, valoraciones, interpretaciones, consultas bibliográficas, definiciones y conceptualizaciones expuestas en el presente trabajo; así cómo, los procedimientos y herramientas utilizadas en la investigación, son de absoluta responsabilidad de la autora del trabajo de integración curricular. Así mismo, me acojo a los reglamentos internos de la Universidad de Investigación de Tecnología Experimental Yachay.

Urququí, junio de 2024.

María Daniela Serrano Larrea

CI: 0105125058

Autorización de publicación

Yo, **MARÍA DANIELA SERRANO LARREA**, con cédula de identidad 0105125058, cedo a la Universidad de Investigación de Tecnología Experimental Yachay, los derechos de publicación de la presente obra, sin que deba haber un reconocimiento económico por este concepto. Declaro además que el texto del presente trabajo de titulación no podrá ser cedido a ninguna empresa editorial para su publicación u otros fines, sin contar previamente con la autorización escrita de la Universidad.

Asimismo, autorizo a la Universidad que realice la digitalización y publicación de este trabajo de integración curricular en el repositorio virtual, de conformidad a lo dispuesto en el Art. 144 de la Ley Orgánica de Educación.

Urcuquí, junio de 2024.

María Daniela Serrano Larrea

CI: 0105125058

Dedication

To my sister, Caro, who always believed in me. She is my biggest support and my inspiration. All my achievements belong to her as much as to me; this work goes for our shared goal to be empowered women and great scientists.

To "MamiIme," a wonderful and feisty woman who has always taken me along the path of learning, discipline, and effort to achieve all my goals, the woman who raised me up to become who I am nowadays, my mommy. And "Joven Leonardo", my dad. The best parents that live could choose for me.

*To my angel Lili, who was my companion for life, and to Rocky, my "Pishito".
To my granny Kika, who always guides and takes care of me from heaven, and my grandpa Coqui, who always cheers me up to follow my dreams.*

To all my family who always support me.

María Daniela Serrano Larrea

Acknowledgment

From the bottom of my heart, I want to thank my sister, Caro, for always supporting me academically and emotionally. Thank you so much, Cariño, for always being there.

To my parents, thank you for raising me to be a kind, honest, and independent woman. Their support has been crucial. Thanks, "MamiIme," for always reminding me, "You are braver than you believe, stronger than you seem, and smarter than you think."

To all the friends Yachay gifted me, especially Mela Aguilar, Cris Rubio, Mabe Silva, Bryan Aldaz, and Daniel Salguero, thank you for supporting, listening, and encouraging me to keep going. Thank you for all the academic and life experiences that helped me grow. You are a fundamental pillar of my university's journey.

To my dear and beloved Carlitos, thank you for coming into my life, for being there by my side during this last time of my university journey, for teaching me completely new life experiences, and for helping me overcome many challenges.

I want to thank my tutor, Doctor Julio Chacón, especially. He illuminated my scientific journey and filled it with knowledge, passion, and new scientific experiences. Thank you so much, Professor Julio!

Finally, I want to acknowledge all the people who guided me in my thesis journey: my co-tutor José Luis Flores; the Yachay laboratory technicians Jhoa P., Jonathan E., and Darwin M.; the pillars of the School of Physical Sciences and Nanotechnology, Dr. Gema G. and Evelyn C.; the Physics technician at USFQ Christian Luciani; and the people who received me at CICSaB in Mexico, Dr. Mildred Q. Dr. Joaset O., and Dr. Selene A.

I will always carry you all in my heart.

María Daniela Serrano Larrea

Resumen

En la actualidad, están surgiendo métodos novedosos y ecológicos para sintetizar nanoestructuras de hard carbon. Esta investigación tuvo como objetivo desarrollar un proceso de síntesis por ablación láser para producir nanomateriales de hard carbon utilizando un residuo de cáscara de coco endémico de Ecuador, de la especie *Parajubaea Cocoides*, como material precursor. El material fue analizado antes y después de la síntesis, mostrando características interesantes; la estructura cambió de una forma granular en el estado inicial a una estructura porosa en las muestras sintetizadas. Además, la técnica de espectroscopía Raman mostró un espectro bien definido para cada una de las muestras sintetizadas, con una relación I_D/I_G de 0.25 y 0.41 para las muestras sintetizadas. También se encontró, mediante XPS, que en los espectros $C1s$, el pico alrededor de 281 eV cambió de tener una baja intensidad en la muestra precursora a un pico muy definido y de alta intensidad en las muestras sintetizadas, mostrando así átomos bien organizados en enlaces $C - C$ con estado degenerado sp^2 . Además, se obtuvieron planos (200) y (002), con XRD, que corresponden a estructuras gráficas; las distancias interplanares estimadas fueron de 0.41 nm, 0.40 nm para las muestras sintetizadas; valores que se comprobaron con el análisis TEM, convergiendo en su totalidad. Como resultado, se dio obtención de una nanoestructura semicristalina en la que se pueden definir arreglos entre capas de grafeno con áreas cerradas rellenas de carbono amorfo a escala nanométrica, dejando algunas vacantes entre ellas; y, a escala macroscópica, se forma una estructura porosa, tal como está reportado en la literatura. Esta nanoestructura es adecuada para el almacenamiento de iones; se propone que las nanoestructuras de hard carbon sean un reemplazo potencial de los ánodos en baterías de estado sólido, sentando las bases para estudios futuros.

Palabras Clave:

Nanoestructuras de Hard Carbon, ablación láser, pirólisis, *Parajubaea Cocoides*.

Abstract

Green novel methods to synthesize carbon nanomaterials are emerging nowadays. This research aimed to develop a laser ablation synthesis process to produce hard carbon nanostructures with an endemic Ecuadorian coconut shell residue, *Parajubaea Cocoides* species, as the precursor material. The material was analyzed before and after synthesis, showing interesting characteristics; the structure changed from a granules-like in the pristine stage to a porous-like structure for the synthesized samples. Moreover, the Raman spectroscopy technique showed a well-defined spectrum for each synthesized sample, with an I_D/I_G ratio of 0.25, and 0.41 for the synthesized samples. It was also found, from *XPS*, that in the *C1s* high-resolution spectra, the peak around 281 eV changed from a low intense peak for the pristine sample to a very sharp and well-defined peak with considerable high intensity in the synthesized samples, thus showing well-arranged atoms in *C – C* with sp^2 degenerated state. Besides, *XRD* analysis showed two predominant planes, (200) and (002), corresponding to graphitic structures; the estimated interplanar distances calculated were 0.41 nm and 0.40 nm for the synthesized samples. Values corroborated with *TEM* analysis, showing precisely the same interplanar distances as calculated in XRD. The research resulted in obtaining a semi-crystalline nanostructure in which there can be defined arrangements between graphene layers with enclosed areas filled by amorphous carbon at the nanoscale, letting some vacancies between them; and, at a macro-scale, it extrapolated to be a porous-like structure, just as predicted and reported in the literature. As this nanostructure has vacancies between the atoms, it makes the structure suitable for storing ions; the hard carbon nanostructures are proposed to be a potential replacement of anodes in solid-state batteries, leaving the fundamentals for future studies.

Keywords:

Hard Carbon nanostructures, laser ablation, pyrolysis, *Parajubaea Cocoides*.

Contents

Contents	vii
List of Tables	ix
List of Figures	x
1 Introduction	1
2 Motivation	7
2.1 Problem statement	7
2.2 Objectives	8
2.2.1 General Objective	8
2.2.2 Specific Objectives	8
3 Theoretical Framework	9
3.1 Carbon-Based Materials	9
3.1.1 Hybridization of Carbon	10
3.1.2 Organic Carbon-based Molecules	14
3.1.3 Carbon Allotropes	18
3.2 Carbon-based Materials Obtantion	21
3.2.1 Chemical Vapor Deposition	21
3.2.2 Pyrolysis	22
3.2.3 Annealing Process	22
3.2.4 Laser Ablation	23
3.3 Natural Carbon-based Materials Precursors	24
3.3.1 Natural Carbon Sources	24
3.3.2 Parajubaea Cocoides	25

3.4	Characterization Techniques	26
3.4.1	Scanning Electron Microscopy	27
3.4.2	Raman Spectroscopy	29
3.4.3	X-ray Photoelectron Spectroscopy	34
3.4.4	X-Ray Diffraction	37
3.4.5	Transmission Electron Microscopy	38
4	Methodology	40
4.1	Sample Preparation	40
4.2	Synthesis of the Hard Carbon Nanostructures	42
4.3	Characterization Techniques	43
4.3.1	Scanning Electron Microscopy	43
4.3.2	Raman Spectroscopy	44
4.3.3	X-Ray Photoelectron Spectroscopy	45
4.3.4	X-Ray Diffraction	46
4.3.5	Transmission Electron Microscopy	47
5	Results and Discussion	48
5.1	Samples	48
5.2	Scanning Electron Microscope	50
5.3	Raman Spectroscopy	55
5.4	X-Ray Photoelectron Spectroscopy	58
5.5	X-Ray Diffraction	60
5.6	Transmission Electron Microscopy	62
6	Conclusions	66
	Bibliography	69

List of Tables

4.1	Description of the particle size of samples used.	41
5.1	Data of Atomic Percentage and Weight Percentage of the pristine sample. .	52
5.2	Data of the peaks obtained of Raman analysis.	56
5.3	Atomic concentration table of samples <i>A</i> , <i>A1T</i> , and <i>A1T75</i> , obtained from XPS measurements.	59
5.4	Peak assignment table of the C1s.	59

List of Figures

3.1	Electronic structure of Carbon.	12
3.2	Lignin, cellulose and starch molecules.	15
3.3	Structure of Carbon allotropes.	18
3.4	Scanning Electron Microscope working function.	27
3.5	Raman Spectroscopy working function.	30
3.6	X-Ray Photoelectron Spectroscopy working function.	35
3.7	X-Ray Diffraction working function.	37
3.8	Transmission Electron Microscopy working function.	39
4.1	Graphical methodology of Sample Preparation.	41
4.2	Synthesis method used: laser ablation.	42
4.3	Scanning Electron Microscopes used.	44
4.4	Horiba LabRAM HR Evolution spectrometer.	45
4.5	VersaProbe III 5000 photoelectron spectrometer.	46
4.6	X-ray diffractometer D8 ADVANCE by Bruker.	46
4.7	Jeol Electron Microscope 2100	47
5.1	Images of samples representing the different stages of the research.	49
5.2	Images of samples before, during, and after the synthesis process.	49
5.3	Images obtained with Phenom ProX G6 Desktop SEM X.	51
5.4	EDS obtained with Phenom ProX G6 Desktop SEM X	51
5.5	SEM of sample A.	53
5.6	SEM images of sample A1T.	54
5.7	SEM images of sample A1T75.	54

5.8	Raman spectra of sample <i>A</i> , <i>A1T</i> , and <i>A1T75</i>	55
5.9	XPS survey and high-resolution C1s spectra of samples <i>A</i> , <i>A1T</i> , and <i>A1T75</i>	58
5.10	XRD diffractogram of samples <i>A</i> , <i>A1T</i> , and <i>A1T75</i>	61
5.11	TEM images of sample <i>A1T</i>	63
5.12	TEM images of sample <i>A1T75</i>	64

Chapter 1

Introduction

Since many industries started, its technology has been obtained by synthetic processes, involving many chemical processes and obtaining its raw materials by damaging ecosystems and polluting the environment. However, the world environment and nature cannot keep spilling and draining its resources. A new approach to obtaining raw materials has started in recent years: taking advantage of the mostly unconsidered resources, such as agricultural bagasse or organic residues. Many types of agricultural waste, such as sugarcane bagasse, corn stover, rice husk, coffee pulp, oil palm empty fruit bunches, soybean hulls, and banana plant waste, can be widely used for many purposes and are valuable and important based on their chemical composition. Those uses include the production of biofuels, paper, bio-based materials like biochar, building blocks, composting, and biogas. As noticeable, many other agricultural and natural residues have not yet been considered and have similar characteristics. The question to solve here is: What is the shared characteristic of those organic materials that makes them valuable and important? The answer relies on their chemical composition, mostly long organic carbon polymers, and their properties and characteristics. These polymers usually correspond to lignin, cellulose, and starch, with a high carbon yield ($> 50wt\%$). Also, lignin, cellulose, and starch are accessible in large quantities in nature and can be replenished by natural cycles, making them renewable resources. Interestingly, the ease of converting these organic materials into new carbon-based materials and nanomaterials opens the path to a new market based on a more economically efficient, eco-friendly, and sustainable production of derived materials, and due to their extensive availability, they are appealing options for sustainable and scalable synthesis processes.

[1, 2] As mentioned, organic molecules such as lignin, cellulose, and starch are suitable precursors for obtaining carbon-based materials. Moreover, these organic molecules exhibit essential characteristics and properties that make them appropriate precursors for synthesizing hard carbon nanostructures. Lignin, cellulose, and starch comprise carbon, which is crucial for forming carbon-based materials and nanostructures. Carbon is well-known for its exceptional stability and hardness, making it a perfect option for producing lasting carbon materials. These molecules show hierarchical structures at various levels, ranging from the large-scale to the nanostructural. These structures can be preserved or altered during synthesis to produce nanostructured carbon materials with specific properties, such as hardness. Furthermore, lignin, cellulose, and starch contain functional groups such as hydroxyl (-OH) and carboxyl (-COOH) groups, capable of performing chemical changes during the synthesis, such as in carbonization processes. The existence of these functional groups can enhance the formation of cross-links while improving the capacity of the resulting carbon materials to maintain specific nanostructures. Furthermore, the exceptional thermal stability of these precursors allows for their conversion into carbon structures and nanostructures without substantial degradation while maintaining precise control over the synthesis process. Due to their ideal porosity conditions, these organic molecules are precursors for forming carbon-based nanostructures. Overall, the combination of abundant availability, carbon-rich composition, hierarchical structure, functional groups, thermal stability, and controlled porosity makes lignin, cellulose, and starch attractive precursors for synthesizing some carbon-based materials and nanomaterials obtained such as graphene, graphite, hard carbon, and even diamond.

Besides, regarding carbon-based materials and nanostructures, graphene, graphite, and diamond have highly ordered atomic arrangements, which means they have crystal structures; however, other carbon-based materials, such as hard carbon, show semi-crystal structures. Due to their properties, these materials have become increasingly demanding and are used in many fields. Graphene, a single-layered arrangement of carbon atoms in hexagonal lattices, has some distinguished properties, such as good mechanical strength, electrical conductivity, and thermal conductivity. This material is usually used in electronics, energy storage devices (such as batteries and supercapacitors), composites, and sensors and is a crucial component in lithium-ion batteries. Moreover, graphite, a multi-layered graphene,

is a demanded material commonly used in pencils, lubricants, and electrodes. Diamond is the hardest known natural material, characterized by its strong covalent bonds between carbon atoms. It is highly valued for its use in jewelry, cutting tools, abrasives, and industrial applications requiring extreme hardness and durability. Nowadays, diamonds can be produced in laboratories with carbon sources; however, those are less economically valued than natural diamonds. Hard carbon nanostructures refer to a type of carbon material characterized by a high degree of disorder and a low degree of crystallinity, making it a semi-crystalline structure. These nanostructures exhibit high porosity, providing ample space for storing ions and making them promising candidates for various applications such as energy storage devices as anode in lithium-ion and solid-state batteries, supercapacitors, catalysis, sensors, and carbon capture technologies. Hard carbon is a recent material that has been used increasingly and is being introduced to all the fields mentioned above.

Moreover, many methods exist to synthesize and produce carbon-based materials, starting from natural sources such as lignin, cellulose, and starch. There is a specific type, the carbonization synthesis method, also known as thermal treatment, which is a novel method for synthesizing carbon-based nanostructures by inducing heating of the organic biomass. [3] These carbonization synthesis methods involve the conversion of carbon-containing precursors into carbon materials by removing non-carbon elements under high temperatures in an inert atmosphere. Thus, lignin, cellulose, and starch carbonization produce carbon materials and nanomaterials with characteristics similar to those of precursor materials, such as well-defined porosity in some cases. The natural characteristics and chemical composition of these initial organic molecules, in conjunction with the parameters of the synthesis processes, can be employed to regulate the size, arrangement, and quantity of the resulting carbon-based nanostructures.

Common carbonization synthesis methods include chemical vapor deposition (CVD), pyrolysis, annealing, and laser ablation. Chemical vapor deposition (CVD) is a synthesis technique where carbon-rich gases are decomposed on a substrate surface at elevated temperatures, leading to the deposition of carbon layers. It is commonly used to produce graphene and carbon nanotubes with controlled thickness and orientation. However, the CVD technique is known to be an expensive method to produce carbon-based materials and nanomaterials. Moreover, annealing is a synthesis method commonly used for devel-

oping carbon structures, specifically graphene and carbon nanotubes. It involves raising the temperature of a material to a precise level and cooling it gradually, typically in a controlled environment. This process facilitates the reorganization of atoms, relieving internal stresses and creating desired structures. Then, pyrolysis is a widely used method where organic precursors are heated in the absence of oxygen to break down into carbon-rich materials. Different carbon materials and nanomaterials, such as carbon black, activated carbon, or hard carbon, can be produced depending on the pyrolysis synthesis conditions. Finally, laser ablation is a carbonization synthesis method that involves irradiating a carbon precursor with a high-energy laser beam in a controlled atmosphere. This leads to the vaporization of functional groups bonded to the organic carbon chains and subsequent carbon atoms condensation onto a substrate. This synthesis method produces carbon nanomaterials such as carbon nanotubes, hard carbon, graphite, and graphene. Overall, the carbonization synthesis methods provide versatility for synthesizing various carbon materials with specific structures, compositions, and properties for various applications, such as energy storage, catalysis, sensors, and materials science.

Consequently, merging the information mentioned above, an industry is trying to introduce eco-friendly production methods for its components, starting from using agricultural waste as raw material, and it is the energy industry, specifically the battery-production industry. Due to the many difficulties of extracting precious metals and minerals that batteries need, scientists have been focusing on finding different precursors for developing new materials and methods for synthesizing and obtaining components for those solid-state batteries. It has been trying to use graphene as a replacement material for anodes in solid-state batteries. However, the production costs are very expensive, and the synthesis processes may not be as green as desirable. Here is when a novel material appears: hard carbon nanostructures. As mentioned, hard carbon nanostructures are semi-crystalline nanostructures with high porosity; their porous nature allows for rapid ion diffusion. Thus, hard carbon is a potential replacement for anodes in solid-state batteries, efficiently storing ions during the charging and discharging and enhancing battery performance and longevity.

This research will emphasize this novel material that can revolutionize solid-state batteries in the energy industry. Hard carbon is a nanomaterial that can store ions at a high capacity and is a potential replacement for conventional anodes of solid-state batteries.

The research first proposes a raw material not used before the *Parajubaea Cocoides* fruit, an endemic Ecuadorian palm species. Due to its null use for anything other than ornamental purposes, this palm species was considered the perfect candidate as the research raw material, proposing a circular economy contributing to a greener synthesis. [4] Looking deep into the literature, there are no studies about the composition of this species. However, compared to similar species as the *Cocos Nucifera*, one of the most common palm species in the world, in theory, the main composition would be cellulose and lignin, the perfect precursor molecules for hard carbon synthesis. In the experimental part of this research, the *Parajubaea Cocoides* fruit, also known as dwarf coconut, was characterized, and the main components were confirmed to be, in fact, cellulose, lignin, and starch.

Moreover, the synthesis method used to produce the hard carbon nanostructures was laser ablation, a laser anneal treatment of the endemic coconut-based biomass, *Parajubaea Cocoides*, to obtain this carbonaceous semi-crystalline nanostructures composed mainly of amorphous carbon in a significant percentage, followed by graphite and graphene at lower concentrations. Hard carbon nanostructures present a high porosity, a shared characteristic of precursor material, making them suitable for many applications, such as storing ions in their structure. [3] The synthesis method proposed was a green procedure, starting from the sample preparation; there were only physical procedures used in clean environments so as not to contaminate the samples and to contribute to the green path of the research. In the synthesis process, specific controlled conditions were used. This green synthesis method promotes a circular economy, as waste products are used to produce the hard carbon semi-crystalline nanostructures, thus not disposing of this waste to avoid increasing garbage in communal garbage dumps and preventing other derived contamination. [3, 5]

Finally, the research converges the suitable precursor raw material with the precise chemical composition, the *Parajubaea Cocoides* fruit, with the right green synthesis method, laser ablation derived from pyrolysis, to obtain hard carbon nanostructures. In addition, the *Parajubaea Cocoides* fruits are an economic precursor contributing to cost-efficient synthesis. Besides, the thermal heating of biomass will help release most of the biomolecules in the raw material, letting the carbon in the sample and forming the carbonaceous structure. The composition of the raw material used, which might correspond to lignin and cellulose, as well as the composition of the hard carbon nanostructures, will be demonstrated in this

research. This will be held by using five different characterization techniques that are Scanning Electron Microscopy (SEM), Raman Spectroscopy, X-ray Photoelectron Spectroscopy (XPS), X-ray Diffraction (XRD), and Transmission Electron Microscopy (TEM).

Chapter 2

Motivation

The world needs to find new approaches to using renewable resources instead of exploiting natural resources that cannot be restored. This necessity is growing exponentially due to global warming and the increasing population. Some agricultural residues are used for eco-friendly industrial processes instead of exploiting natural resources. Some of those, such as sugarcane bagasse, corn stover, rice husk, coffee pulp, oil palm empty fruit bunches, soybean hulls, and banana plant waste, are being taken advantage of; however, many other natural residues are not.

Science needs to solve a wide variety of problems worldwide. Specifically, Ecuador is currently in an energetic crisis. Thus, it is necessary to find new solutions to this problem. This research noticed a specific problem related to the energy industry: it is seeking new methods and raw materials to produce different components with the same properties as conventional ones. Thus, this research focuses on finding a different raw material to produce hard carbon nanostructures using a green synthesis method.

2.1 Problem statement

The green synthesis of hard carbon nanostructures is the main objective of this research. Expanding the idea, it was proposed a synthesis method, laser ablation, derived from thermal treatment or carbonization synthesis methods, in order to produce hard carbon nanostructures. Additionally, this research proposes the use of an endemic Ecuadorian palm residue as the raw material; this palm species is the *Parajubaea Cocoides*; specifically, it is proposed to use the shell or husk of the fruit of this palm (also known as dwarf

coconut). Two main reasons justify the usage of dwarf coconut as the raw material, and those are using an unconsidered residue or waste to implement a circular economy in the research and showing that hard carbon nanostructures can be synthesized from an organic precursor containing organic molecules such as lignin, cellulose, and starch. Additionally, this research proposes laser ablation as the synthesis method due to the necessity to show the scalability of the hard carbon nanostructures production, with reduced costs and by being an eco-friendly process.

2.2 Objectives

2.2.1 General Objective

- Developing a green synthesis method to obtain carbon-based nanostructures by laser ablation of biomass waste from Ecuadorian endemic materials.

2.2.2 Specific Objectives

- Implementing Ecuadorian endemic bio-waste as a carbon precursor for synthesizing hard carbon nanostructures.
- Developing an optimized methodology process to obtain hard carbon nanostructures via laser ablation.
- Determining the origin and classification of the organic source of hard carbon to be implemented.
- Characterizing the obtained hard carbon nanostructures to determine their morphology, crystallinity, structure, and chemical composition.

Chapter 3

Theoretical Framework

This chapter overviews the concepts necessary to comprehend the "Green Synthesis of Hard Carbon Nanostructures." First, it is necessary to understand the carbon atom characteristics, its different types of hybridization, which bonds each can form, and the molecules and materials that can be derived from it. Thus, understanding the structure of some carbon allotropes, such as graphene, graphite, diamond, and hard carbon, and the structure of some molecules containing carbon, such as lignin, cellulose, and starch, to relate between why the raw material precursor was used and how hard carbon nanostructures can be formed. Moreover, with this knowledge, the path to the different synthesis methods is taken to understand how hard carbon nanostructures were obtained and the conditions for the ideal formation of the material, as this research emphasizes the laser ablation synthesis technique derived from the pyrolysis process. Finally, some characterization techniques must be used to ensure the formation of hard carbon nanostructures. This research employed five different characterization techniques to determine the composition of the material; therefore, the fundamentals of the characterization techniques will be presented to understand and analyze each step of the synthesis, how the material was formed, its chemical composition, and its properties.

3.1 Carbon-Based Materials

Carbon is known as the fundamental element for life on Earth. The role of the carbon atom results from its capacity to form bonds with itself and with a wide range of elements in an infinite number of different types. The wide variety of organic and inorganic com-

pounds containing carbon leads to diverse chemical and physical properties. Carbon-based materials enclose diverse substances with unique structures and properties due to the ability of carbon to form multiple allotropes, chemical bonds, and hybridization states. In addition, those carbonaceous compounds may form various structures, carbon allotropes corresponding to carbon-only-based structures, and other carbon structures build up with other elements from the periodic table. Due to their exceptional properties and versatility, these materials have widespread applications in electronics, science, medicine, and energy. [6] This research focuses on four carbon allotropes: graphene, graphite, diamond, and amorphous carbon, as well as three punctual organic carbon-based molecules: starch, lignin, and cellulose. [7]

The carbon atom has special characteristics, such as its atomic number being 6, meaning that on its ground state, it has two electrons in the $1s$ orbital and four in the $2s$ and $2p$ orbitals. As atoms always look for a stable noble gas electronic configuration, the uncompleted $2p$ orbital will allow carbon to form up to four covalent bonds, sharing electrons with other atoms and completing its outer shell. [8]

3.1.1 Hybridization of Carbon

The concepts of ground state, excited state, and hybridization must be understood to understand the electronic structure of carbon atoms as seen in Figure 3.1. The ground state of the carbon atom is its lowest energy state, where electrons occupy the lowest available energy levels according to the Aufbau principle and the Pauli exclusion principle. [9, 10] In the ground state, carbon atoms naturally have two electrons in the $1s$ orbital and two electrons in the $2s$ orbital, with the remaining two electrons occupying the $2p$ orbitals. The ground state electronic configuration of carbon is $1s^2 2s^2 2p^2$. [11] On the other hand, the excited state is when a carbon atom absorbs energy, such as through the excitation of photons or heat. It can induce an excited state where electrons are promoted to higher energy levels. In the excited state, electrons may temporarily occupy higher energy orbitals beyond their usual ground state configuration. For example, in the case of carbon, one or more electrons may be excited from the $2s$ orbital to one of the $2p$ orbitals, resulting in an excited electronic configuration. However, the excited state is typically unstable, and the atom will eventually return to its ground state by releasing the absorbed energy, often in

the form of light. [12] Finally, hybridization, or low energy state, refers to mixing atomic orbitals to form new hybrid orbitals better suited for bonding in molecules.

Carbon atoms commonly undergo hybridization to form covalent bonds with other atoms or with carbon atoms as well. The hybridization states of carbon are sp , sp^2 , and sp^3 , which result from the mixing of the $2s$ and $2p$ orbitals. These degenerated orbitals, resulting from the hybridization, have lower energy than the individual atomic orbitals and are used by carbon to form covalent bonds with other atoms in molecules. Hybridization allows carbon to achieve stable configurations and form diverse molecular structures, contributing to organic and inorganic compounds found in nature and synthesized materials in laboratories. [11]

On the other hand, two types of bonds could be present in the different hybridizations; those are σ and π . These bonds are fundamental to covalent bonding in molecules. Sigma bonds are created when atomic orbitals directly overlap, allowing for straight electron sharing between atoms. On the contrary, pi bonds are formed when parallel p orbitals overlap side-to-side. Sigma bonds, prevalent in single bonds as $C - C$ and $C - H$, are strong, allowing free rotation. They often involve hybridized orbitals like sp , sp^2 , or sp^3 . Weakly than sigma bonds, Pi bonds restrict rotation and are found in double and triple bonds like $-C = C-$ and $-C \equiv C-$, formed by unhybridized p orbitals. Both types contribute to molecular stability, shape, and properties, shaping their reactivities and electronic structures. In this research, it is important to have the above information clear to recognize the different carbon hybridizations that might be present in hard carbon nanostructures and their precursor material and compare how the synthesized material has changed.

***sp* Hybridization**

In carbon atoms, this hybridization is observed when one orbital s and one orbital p in the same shell are mixed to form two new degenerated orbitals. The new orbitals formed are called sp hybrid orbitals. The ground state of the carbon atom corresponds to the complete electronic configuration, which is characterized by $1s^2 2s^2 2p^2$. The $1s$ orbital is fully occupied with two electrons, as is the $2s$ orbital. The two remaining electrons are in the $2p$ orbitals, with one electron in each of the three available $2p$ orbitals ($2p_x$, $2p_y$, and

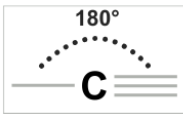
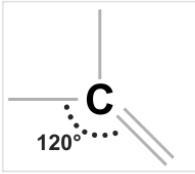
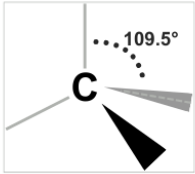

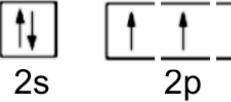
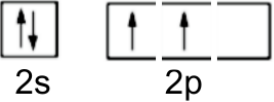


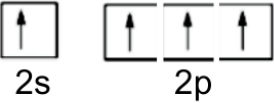
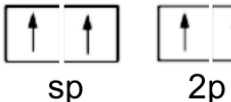
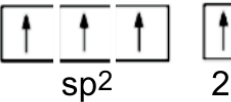

Hybridization	sp	sp^2	sp^3
Geometry			
Ground State			
Excited State			
Hybridization (Low Energy State)			

Figure 3.1: Electronic structure of Carbon atom.

$2p_z$). This configuration represents the lowest energy state of the carbon atom. Besides, when a carbon atom goes through sp hybridization, one of the $2s$ electrons is promoted to the vacant $2p$ orbital, resulting in an excited state. This promotion of an electron requires energy, usually in the form of heat or light. As a result of this excitation, the carbon atom now has an electronic configuration with one electron in the $2s$ orbital and three electrons in the $2p$ orbitals. Then, in the hybridization process, the $2s$ orbital and one of the $2p$ orbitals (mostly the $2p_z$ orbital) combine to form two sp degenerated orbitals. These sp degenerated orbitals are oriented linearly, with a bond angle of 180° between them, as seen in Figure 3.1. The remaining two $2p$ orbitals ($2p_x$ and $2p_y$) remain non-degenerated and perpendicular to the plane of the sp hybrid orbitals. The sp degenerated orbitals have lower energy than the original $2s$ and $2p$ orbitals and are used by the carbon atom to form one triple and one single bond, corresponding to two π bonds, and one σ bond and one σ bond respectively; also, two σ bonds remain from the non-degenerated orbital. [13, 11, 8]

A characteristic example of this hybridization is dimerized carbon rings with alternating single and triple bonds – $C \equiv C$ –. Another characteristic example of this hybridization is carbon dioxide (CO_2), a linear triatomic molecule. Each carbon atom undergoes sp hybridization in carbon dioxide to form two sp degenerated orbitals. Each sp hybrid

orbital forms a sigma (σ) bond with an oxygen atom by overlapping their $2p$ orbitals. Additionally, two pi (π) bonds are formed by overlapping the non-degenerated p orbitals of carbon and oxygen atoms ($-O = C = O-$). [14] When the hybridization sp has taken place, the resulting geometry is a linear geometry with an angle of 180° as seen in Figure 3.1. [11]

sp^2 Hybridization

As well as in sp hybridization, the ground state of the carbon atom and the excited state occur similarly. However, concerning sp^2 hybridization, it occurs when an s orbital and two p orbitals from the same atom-shell combine to create three degenerated orbitals that will result in an sp^2 hybrid orbitals. The $2s$ orbital and two of the $2p$ orbitals ($2p_x$ and $2p_y$) combine to form three sp^2 hybrid orbitals. The remaining $2p_z$ orbital stays non-degenerated and perpendicular to the plane of the sp^2 hybrid orbitals, as it does not participate in the hybrid process. This degeneracy, or hybridization, facilitates the formation of stable σ bonds with other atoms; the sp^2 hybridization can form three σ bonds and one π bond. The formation of sp^2 hybrid orbitals results in a lower energy state than the original atomic orbitals. These hybrid orbitals are then available for bonding with other atoms to form covalent bonds. The carbon atom now has three sp^2 hybrid orbitals and one unhybridized $2p_z$ orbital. As shown in Figure 3.1., the sp^2 hybridization will be arranged in a certain geometry forming a 120° angle, and it is the trigonal planar geometry. [11]

Graphene is a common carbon structure with hybridization sp^2 . Graphene consists of a two-dimensional structure of carbon atoms forming a honeycomb lattice. The atoms form covalent bonds with three adjacent carbon atoms, resulting in a trigonal planar configuration. The configuration results in a hexagonal lattice structure where carbon-carbon bonds connect the atoms at angles of 120° . This structure is recognized because, between two carbon atoms, two σ bonds are present.

sp^3 Hybridization

The sp^3 hybridization of a carbon atom involves transforming from its ground state to an excited state and then to a hybridization state. Initially, in the ground state, a carbon atom has an electronic configuration of $1s^2 2s^2 2p^2$, with two electrons in the $1s$ orbital,

two in the $2s$ orbital, and one each in the $2p_x$ and $2p_y$ orbitals. Upon receiving energy and transitioning to an excited state, one of the electrons from the $2s$ orbital moves to the vacant $2p_z$ orbital, resulting in an excited state configuration of $1s^2 2s^1 2p_x^1 2p_y^1 2p_z^1$. In the subsequent hybridization process, all four valence orbitals (one $2s$ and the three $2p$) combine to form four sp^3 degenerated orbitals. It is also known as the trigonal pyramidal geometry. [11] These sp^3 degenerated orbitals are oriented in a tetrahedral arrangement around the carbon atom, with bond angles of approximately 109.5° between them, see Figure 3.1.. Each sp^3 hybrid orbital contains one unpaired electron ready for bonding. The formation of sp^3 hybrid orbitals represents a lower energy state than the original atomic orbitals. In terms of bonding, each sp^3 hybrid orbital forms a σ bond with another atom through head-on overlap. Since all available orbitals participate in σ bonding, no non-degenerated p orbitals remain for forming π bonds. Consequently, in sp^3 hybridization, a carbon atom can form four σ bonds and no π bonds. This hybridization state is commonly observed in compounds like methane (CH_4) and ethane (C_2H_6), where each carbon atom forms four single σ bonds with hydrogen atoms.

In this hybridization, some examples are that diamond is the most common structure when referring to sp^3 hybridization and organic compounds with carbon organic chains as in cellulose, starch, or lignin structures. Adding to it, another particular nanostructure shows sp^3 hybridization, which is hard carbon.

3.1.2 Organic Carbon-based Molecules

Naturally occurring organic molecules, such as carbohydrates and polymers like lignin, are vital components of the biological world, providing essential functions of living organisms in organization, operation, and energy processing. Carbohydrates, which include simple sugars such as glucose and complex polysaccharides like cellulose, are crucial in providing energy and serving as structural components in living organisms. Glucose is an essential energy substrate for cellular respiration, supplying the necessary fuel for metabolic processes. Polysaccharides, like cellulose, are highly prevalent in plant cell walls and provide strong structural support and rigidity to plant cells. Likewise, starch, a carbohydrate found in plants, functions as a storage unit for energy that can be used for future metabolic requirements. On the other hand, polymers such as lignin, a complex organic compound present

in the cell walls of plants, confer strength and rigidity to the cell walls, thereby enhancing the overall structural stability of plants. Lignin is a protective barrier against pathogens and facilitates the movement of water and nutrients within plant tissues. Carbohydrates and polymers, such as lignin, combine to create the fundamental framework of plants. This structure offers the necessary support, protection, and functionality for the plants to grow, develop, and survive in different environments. Their abundance and variety emphasize their importance in the complex chain of life on Earth.

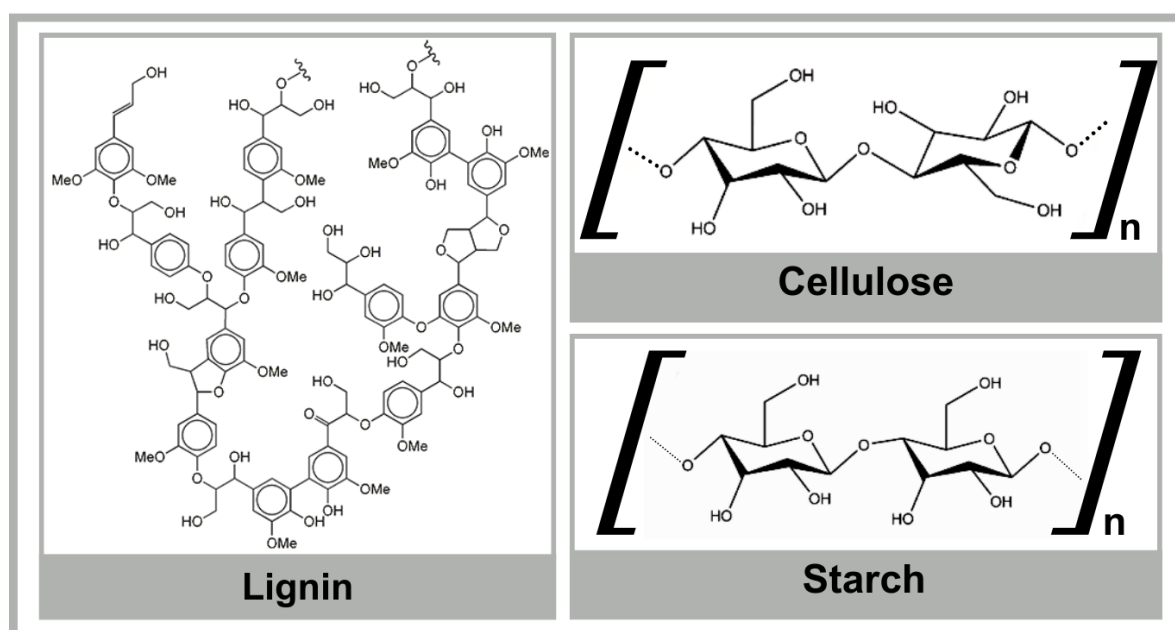


Figure 3.2: Lignin, cellulose and starch molecules.

Cellulose

Cellulose is a polysaccharide and one of the most abundant biomolecules in the natural world. The structure comprises elongated glucose monomer chains connected by β - *glycosidic* bonds; this makes a linear glucose structure made out of n glucose units. (See Figure 3.2) [15] Cellulose comprises glucose molecules arranged in repeating units in a linear chain connected via glycosidic bonds between their C_1 and C_4 positions. Its molecular formula is $(C_6H_{10}O_5)_n$. Carbon atoms in glucose molecules create covalent bonds with oxygen, hydrogen, and neighboring carbon atoms. Carbon bonds in cellulose show to be sp^2 hybridization around the carbon atoms in each glucose unit, leading to a tetrahe-

dral structure. [16] The hydroxyl ($-OH$) groups of the glucose molecules are positioned alternately, enabling hydrogen bond formation between neighboring chains. In addition, cellulose carbon atoms usually exhibit sp^3 hybridization, forming tetrahedral bonds with other atoms. Every carbon atom in cellulose creates single bonds with other carbon atoms or elements like hydrogen and oxygen, creating a three-dimensional structure. [17, 18]

Cellulose possesses exceptional strength and rigidity due to hydrogen bonding, making it an outstanding structural material. Cellulose is predominantly located in the cell walls of plants, serving as a crucial component that imparts structural support and stiffness to plant cells, thereby enhancing the overall strength of plant tissues. It is especially abundant in wood, cotton fibers, shells, and plant stalks. Cellulose is widely utilized in diverse industries due to its abundant availability and distinctive characteristics. Because of their ability to decompose naturally and their renewable characteristics, cellulose is a highly adaptable and essential molecule with various uses in various industries, agriculture, and daily activities. Cellulose, derived from natural sources, is extracted and transformed into paper, cardboard, and other cellulose-based products; cellulose can also be a precursor for synthesizing carbon-based materials such as graphene, graphite, and hard carbon. Furthermore, This emphasizes its significance in the global economy and efforts towards environmental sustainability. [16]

Lignin

Lignin is a complex organic macro molecule that is present in the cellular structures of plants. It is vital in providing structural support and rigidity to plant tissues. (See Figure 3.2) Lignin consists of phenylpropanoid units, mainly coniferyl, sinapyl, and p-coumaryl alcohols, which are connected by different functional groups, such as ether and $C - C$ bonds. The rings phenylpropane units have mainly aromatic character. It is important to mention that, unlike starch or cellulose, lignin has nitrogen atoms in its structure. [19] The bonds are usually sp^2 hybridized, leading to planar and tetrahedral geometry surrounding the carbon atoms, which can be $C - C$ single or double bonds. [20]

The unique polymer arrangement of lignin contributes to its strength and durability against deterioration. This molecule is highly prevalent in hardwood and softwood trees, grasses, roots, plant husks, and shells. lignin is a structural component and protec-

tive barrier against pathogens, pests, and environmental stresses, enhancing plant defense mechanisms. [19] Besides, due to its diverse applications, lignin has attracted considerable attention as a renewable and sustainable resource. It is frequently employed as a primary substance in manufacturing adhesives, resins, and binders in various industries, including paper and pulp, construction, and composite materials. The uses of materials derived from lignin are being investigated as additives in concrete and asphalt mixtures to enhance their strength and durability. Furthermore, lignin can be transformed into carbon-based materials using biochemical and thermochemical conversion methods, offering a promising renewable substitute for common precursors. In summary, lignin is a valuable and adaptable part of plant biomass with various industrial uses and the potential to contribute to sustainable development and environmental conservation. [20]

Starch

Starch is a polysaccharide comprised of glucose molecule units connected by α – *glycosidicbonds*. It serves as the main storage form of energy in plants, acting as a reservoir of glucose that can be easily used when necessary. Starch molecules are composed of two primary polysaccharides, named amylose and amylopectin. Amylose is a chain-like molecule made up of glucose units connected by α 1 – 4 *glycosidicbonds* glycosidic bonds, whereas amylopectin is a more complex molecule with occasional α 1 – 4 *glycosidicbonds*, leading to a highly branched structure. (See Figure 3.2) Glycosidic bonds connect glucose units by linking carbon atoms, creating straight or branched chains based on the starch type. The corresponding general molecular formula of starch is $(C_6H_{10}O_5)_n + (H_2O)$ [21, 15] Carbon bonds in starch exhibit sp^2 hybridization around the carbon atoms in each glucose unit, leading to a tetrahedral structure. Carbon bonds in starch are essential for its structure and function as a plant storage polysaccharide. They store energy that can be easily broken down to release glucose for metabolic activities. [22]

Starch is frequently present in plant storage organs like seeds, tubers, and roots, where it acts as an energy source for germination, growth, and reproduction. Starch-rich foods encompass grains (such as rice, wheat, and corn), tubers (such as potatoes and yams), and legumes (such as beans and peas). Starch is a plant food reserve extensively used in various industrial applications; this molecule is extensively employed as a thickening

agent, stabilizer, and gelling agent in the food industry. Its purpose is to enhance the texture, viscosity, and mouthfeel of products such as soups, sauces, dressings, and baked goods. [21] Starch is also used to manufacture biodegradable plastics, adhesives, and pharmaceuticals. In addition, sugars derived from starch can undergo fermentation to generate bioethanol, a renewable and eco-friendly substitute for fossil fuels. Starch is a highly adaptable and essential molecule with great biological, nutritional, and industrial significance. Its wide range of applications and relevance in different aspects of human life make it an indispensable compound. [22]

3.1.3 Carbon Allotropes

Carbon allotropes are distinct structural configurations of carbon atoms, each with unique arrangements of carbon atoms resulting in distinct properties and applications. Some common carbon allotropes include graphite, diamond, graphene, and hard carbon. See Figure 3.3..

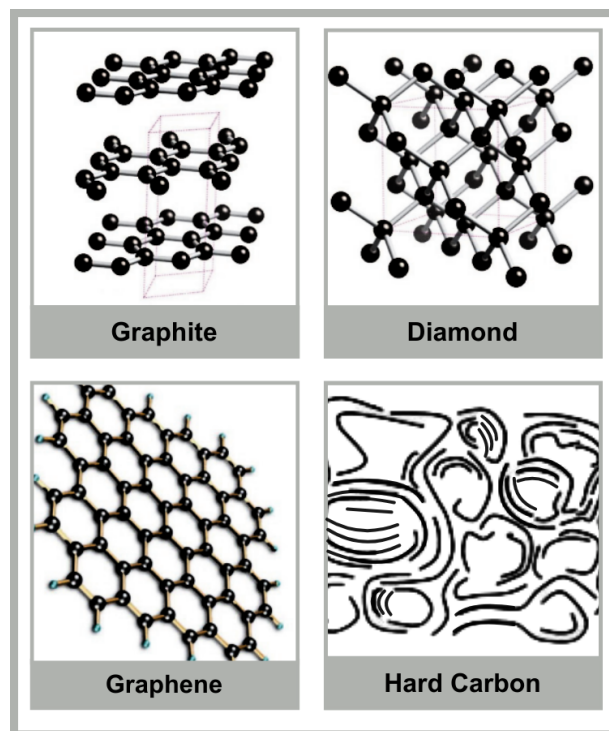


Figure 3.3: Structure of Carbon allotropes.

Graphene

Graphene consists of a single layer of carbon atoms organized in a two-dimensional hexagonal lattice, also known as a honeycomb pattern. See Figure 3.3.. Carbon bonds in graphene are covalent and mainly sp^2 hybridized, with each carbon atom creating three σ bonds with three adjacent carbon atoms. The σ bonds are created by merging sp^2 hybrid orbitals, leading to a strong and enduring arrangement. Graphene displays conjugated π bonds created by overlapping unhybridized p orbitals that are perpendicular to the plane of the graphene sheet. These π bonds in graphene enhance its electrical characteristics, increasing electron mobility and conductivity. [23]

It is widely recognized for its outstanding mechanical, electrical, and thermal characteristics, making it a highly promising material for various applications, such as electronics, energy storage, and composite materials. Graphene can be produced using mechanical exfoliation and chemical vapor deposition. [24]

Graphite

Graphite is a three-dimensional crystalline allotrope of carbon characterized by layers of graphene sheets stacked and held together by weak Van der Waals forces. As seen in Figure 3.3.. All carbon atoms in graphite create strong σ bonds with three adjacent carbon atoms in the same layer, leading to a flat structure. The σ bonds are created by sp^2 hybridization, in which each carbon atom has three valence electrons shared between two sp^2 hybrid orbitals and one non-degenerated p orbital. These non-degenerated p orbitals of carbon atoms in graphite overlap to create delocalized π linkages above and below the layers of carbon atoms. The π bonds in graphite are responsible for its distinctive characteristics, including electrical conductivity and lubricating qualities. Its smooth and slick consistency distinguishes it, and it is frequently employed as a lubricant, graphite for pencils, and in diverse industrial uses such as refractories and batteries. [25]

Diamond

Diamond is a carbon allotrope with a crystal structure known for its extremely hard nature, ability to let light pass through, and efficient heat transfer. The structure of this material is composed of carbon atoms organized in a three-dimensional lattice of tetrahedral units.

Each carbon atom forms strong sigma (σ) bonds with four adjacent carbon atoms through covalent bonding. Diamond is an exceptionally stable and rigid structure, which makes it the most resilient naturally occurring material. Diamond carbon atoms display sp^3 hybridization, wherein each carbon atom combines one s orbital and three p orbitals to create four sp^3 degenerated orbitals. The degenerated orbitals of carbon atoms overlap with those of neighboring carbon atoms, forming strong sigma bonds that give rise to the diamond lattice structure. [26]

Diamond possesses exceptional properties that make it highly suitable for various industrial uses, such as cutting tools, grinding wheels, and precision machining abrasives. Additionally, it finds application in jewelry due to its exceptional brilliance and durability, greatly enhancing its value. Diamonds are commonly located in kimberlite pipes, which are volcanic formations responsible for transporting diamonds from the mantle of the Earth to the surface. The distinctive structure, composition, and properties of diamond make it a valuable and adaptable substance, suitable for various applications in industry, technology, and luxury goods. [27]

Hard Carbon

Hard carbon is a carbon-based material known for its variable composition, consisting mainly of amorphous carbon with lesser amounts of graphite and graphene. As, in this research approach, hard carbon is derived from an organic precursor, thanks to the rearrangement of the carbon bonds present in the precursor, the final hard carbon nanostructures will comprise amorphous carbon as well as crystalline structures or allotropes of carbon, such as graphite and graphene. Amorphous carbon is the main constituent of hard carbon and is characterized by a lack of long-range order in its atomic structure, resulting in a disordered, non-crystalline structure. As amorphous carbon consists of carbon atoms organized randomly, without a defined pattern or recurring unit cell, it will present various structural arrangements, combining sp^2 hybridization state. Amorphous carbon contains a variety of carbon-carbon, carbon-hydrogen, and carbon-oxygen bonds; the irregular configuration of carbon atoms enhances the hardness of the material and the ability to resist deformation. [24, 28]

On the other hand, hard carbon may contain trace amounts of graphite and graphene.

[29] The layers add crystallinity to the material and enhance its properties. Small amounts of hard carbon may include graphene, a single layer of carbon atoms arranged in a two-dimensional honeycomb lattice, and graphite. Graphene sheets incorporated in the rigid carbon matrix can improve mechanical strength and electrical conductivity. [30]

Finally, hard carbon is a nanostructure that has a combined hybridization sp^2 crystalline and amorphous. This makes the hard carbon structure a semi-crystalline nanostructure. This arrangement leads hard carbon to present porosity, leaving vacancies between the structure. This particular characteristic is highly valued because the uses of hard carbon are mostly based on it. For example, hard carbon is suitable for ion storage due to its porosity. It can then be used as a replacement for anodes in solid-state (conventional lithium-ion) batteries for the energy industry. [30]

3.2 Carbon-based Materials Obtention

Many different synthesizing techniques can be used to obtain Hard Carbon Nanostructures. It is important to understand the concepts behind chemical vapor deposition, pyrolysis, annealing process, and laser ablation synthesis methods and their differences. In this research, the laser ablation synthesis technique was applied for various reasons, which will be included in the following section.

3.2.1 Chemical Vapor Deposition

Chemical Vapor Deposition (CVD) is a common technique for producing hard carbon nanostructures. Carbon-containing gases are introduced into a reaction chamber where they undergo chemical reactions to deposit carbon atoms onto a substrate, forming nanostructures. [31] The substrate is positioned in a reaction chamber, which is subsequently evacuated to establish a vacuum for eliminating impurities, and carbon-containing precursor gases like methane (CH_4), acetylene (C_2H_2), or ethylene (C_2H_4) are added to the reaction chamber. These gases provide the carbon atoms needed for the deposition process. [32]

Activation involves heating the precursor gases to high temperatures, usually between $600^\circ C$ and $1000^\circ C$. The thermal energy disrupts the bonds in the precursor molecules,

releasing carbon atoms. Deposition involves carbonaceous species adhering to the substrate surface and initiating the growth of nanostructures. The synthesis process parameters, including temperature, pressure, gas flow rates, and substrate properties, are meticulously controlled to attain the desired properties and morphology of the carbon nanostructures. [33]

3.2.2 Pyrolysis

Pyrolysis is a common synthesis method for producing hard carbon nanostructures by exposing precursor materials with high carbon yield to high temperatures without oxygen. Carbon-containing precursors are chosen for their capacity to decompose and produce carbon-rich residues at high temperatures. Possible precursors include organic compounds like polymers, hydrocarbons, or biomass-derived materials. The precursors are placed in a pyrolysis reactor, usually a sealed chamber or furnace. Inert gases like nitrogen or argon purge the reactor, creating an oxygen-free environment to prevent the combustion of the precursors. Based on the precursor and intended product, the reactor is heated to elevated temperatures, usually from 500°C to 1500°Celsius. [34]

Heating the precursors drastically results in thermal decomposition, which releases volatile byproducts like gases and liquids, forming carbon-rich residues. The residues are carbon atoms bonded in different structural configurations, determined by the precursor composition and decomposition conditions. Carbon-rich residues produced from pyrolysis act as nucleation sites for the growth of nanostructured carbon materials. Factors like precursor composition, pyrolysis temperature, heating rate, and reaction time influence the development and shape of carbon nanostructures. Once the pyrolysis reaction time has elapsed, the reactor is cooled, and the carbon nanostructures are gathered from the reactor chamber. The gathered nanostructures might need additional purification and processing to eliminate any remaining impurities and enhance their properties. [35]

3.2.3 Annealing Process

Annealing is a frequently employed process in producing hard carbon nanostructures to alter the characteristics and arrangement of carbon materials. Carbonaceous materials like

carbon black, graphene oxide, or carbon nanotubes are commonly utilized as precursor materials for creating hard carbon nanostructures. The carbon precursors undergo annealing, a process in which they are heated to high temperatures in a controlled environment. The annealing temperature and atmosphere may vary based on the final nanostructures and desired characteristics. The carbon precursors, particularly precursors, are slowly heated to the annealing temperature to avoid thermal shock and ensure even heating.[36] Once the desired annealing temperature is reached, the precursors are maintained for a specific period to facilitate structural rearrangement and transformation.

Due to diffusion and thermal activation processes, carbon precursors experience structural rearrangement during annealing. This process can remove the functional groups of the precursor material, defects, or impurities, forming hard carbon nanostructures with enhanced properties. Annealing can sometimes induce the graphitization of carbon precursors, creating graphitic structures characterized by organized carbon atom arrangements. This procedure can improve the electrical conductivity, mechanical strength, and thermal durability of the nanostructures produced. Once the annealing process is finished, the samples are slowly cooled to room temperature to avoid sudden cooling-induced stresses. [37]

3.2.4 Laser Ablation

Laser ablation is a method that produces hard carbon nanostructures by directing a high-power laser beam onto a carbon precursor in a controlled environment. To understand the laser ablation process for creating hard carbon nanostructures, it is necessary to merge in the following process. A carbon target or a precursor material, such as a solid graphite rod, a carbon film, or a carbon-containing substrate, is readied for laser ablation. In the group of carbon-containing substrates, an organic waste with a high carbon yield could be present, such as lignin, cellulose, starch, or the three mentioned precursors in the same material. The quality of the precursor and its properties significantly influence the characteristics of the synthesized nanostructures; for instance, if the precursor material presents a high porosity, it is almost assured that the synthesized hard carbon nanostructures will also present this property. The carbon precursor is positioned in a reaction chamber containing a regulated atmosphere, such as inert gases like argon or helium; however, it may also be

done in a not completely enclosed environment. A high-intensity laser beam is concentrated on the surface of the carbon precursor, leading to quick heating and focused vaporization of the organic radicals present or added to the carbon material precursor. In addition, the high temperature of the laser beam vaporizes the carbon precursor surface, forming a plasma plume that includes vaporized carbon species, clusters, and nanoparticles. The laser-induced plasma plume quickly expands from the target surface because of the intense temperature and pressure differences. Supersaturated carbon species undergo nucleation and condensation to form nanostructures as the expanding and cooling plasma plume.[38]

Nucleation and growth processes happen quickly in the plasma plume, creating nanostructures such as nanoparticles, graphite, graphene flakes, and amorphous carbon. The hard carbon nanostructures are created and then placed on a substrate in the reaction chamber or collected on a suitable surface. A thin film can be applied to the substrate or collector to enhance adhesion and regulate the alignment of nanostructures. The characteristics and shape of the produced nanostructures are customized by precisely managing parameters like laser power, wavelength, pulse duration, repetition rate, gas pressure, and target composition. [39]

3.3 Natural Carbon-based Materials Precursors

As mentioned, hard carbon nanostructures need material precursors with a high carbon yield on their composition. Thus, biomass is a suitable option when synthesizing hard carbon nanostructures.

3.3.1 Natural Carbon Sources

Biomass is organic matter from organisms like plants, animals, and microorganisms. Biomass is a beneficial precursor material for hard carbon nanostructures because of its natural abundance, renewable characteristics, and varied chemical composition. [40] Biomass consists mainly of carbon, hydrogen, and oxygen, as well as smaller quantities of elements like nitrogen, sulfur, and minerals. Biomass composition varies based on sources, such as agricultural residues, forestry, algae, and solid waste. Biomass materials have a sophisticated hierarchical structure that includes organic components like cellulose, hemicellulose,

lignin, proteins, lipids, and sugars. These organic components are a valuable source of carbonaceous precursors for creating hard carbon nanostructures. [32]

Specific molecules present in biomass, like lignin, starch, and cellulose, contain high levels of carbon and can be used as ideal precursor materials for producing hard carbon nanostructures. Carbon-rich precursors undergo thermal decomposition and rearrangement during carbonization processes, such as pyrolysis or laser ablation, forming carbonaceous derivatives. Precursor materials derived from biomass provide a sustainable and renewable option compared to other carbon sources, such as the ones based on fossil fuels. Finally, hard carbon nanostructures can be produced environmentally friendly using biomass waste precursors, which helps reduce greenhouse gas emissions. [41]

Moreover, these natural carbon sources can take advantage of organic waste derived from agricultural or ornamental industries, also called bio-waste. There are uncountable examples of this mentioned bio bio-waste, such as sugarcane bagasse, corn stover, rice husk, coffee pulp, oil palm empty fruit bunches, soybean hulls, and banana plant waste. Due to its chemical composition, this bio-waste is highly valued. These materials may contain lignin, cellulose, and/or starch, with a carbon yield higher than fifty percent, making them suitable for producing hard carbon nanostructures.

3.3.2 Parajubaea Cocoides

This research considered *Parajubaea Cocoides* fruit, an Ecuadorian endemic palm species, the precursor material for producing hard carbon nanostructures. It is important to introduce this species. There are approximately 2600 species and over 200 genera of palms worldwide, all belonging to the *Arecaceae* family, also known as the *Palmae* family. This family contains multiple genera, including one specific to the Andean Region that prospers at unusual altitudes, distinct from the typical Palm genus.[42] The *Parajubaea* genus is native to South America and typically found at elevations ranging from 1700 to 3400 meters above mean sea level (MAMSL). [43] It includes three distinct species: *Parajubaea Torally* (*P. Torally*, also known as *janchicoco*), *Parajubaea Shunka* (*P. Sunkha*), and *Parajubaea Cocoides* (*P. Cocoides*). *P. Torally* and *P. Shunka* are native to Bolivia, whereas *P. Cocoides* is native to Ecuador and southern Colombia. These three species hold ornamental importance in their specific regions. [44] *Parajubaea Cocoides* is also called *Cumbé Co-*

conut, *Parajubaea Cocoides* Burret, *Cocoides* Palm, or Andean Mountain Coconut. This palm species is native to the Andean region of Ecuador and Colombia. [45]

However, as not much literature is reported about this palm species, a characterization to approximate the coconut shell composition is also presented in this research. Compared with the *Cocos Nucifera* species, the conventional coconut palm species, whose fruit contains more than 35 % of lignin and cellulose in its structure, the *Parajubaea Cocoides* fruit is expected to present lignin and cellulose in their structure. [46, 15] Thus, the *Parajubaea Cocoides* fruit is expected to have a very similar chemical composition to the *Cocos Nucifera* fruit, because they come from the same family and sub-family, *Arecaceae* and *Arecoideae*. [18]

3.4 Characterization Techniques

Scanning Electron Microscopy (SEM), Raman Spectroscopy, X-ray Photoelectron Spectroscopy (XPS), X-ray Diffraction (XRD), and Transmission Electron Microscopy (TEM) are the characterization techniques used in this research for characterizing hard carbon nanostructures. Due to their complementary character and ability to provide a complete understanding of the structure, composition, morphology, and properties of materials, these techniques are suitable for use in hard carbon nanostructure characterization.

SEM offers high-resolution imaging capacities, allowing for surface morphology and topography visualization. Raman Spectroscopy provides information about the vibrational modes of carbon atoms, showing structural defects and bonding configurations present in hard carbon nanostructures. XPS allows the analysis of the surface chemistry and elemental composition, helping identify functional groups and impurities. XRD is crucial for determining the crystallinity structure and phase purity of hard carbon nanostructures. At the nanoscale, TEM provides detailed information about the internal structure, including crystallographic orientation, boundaries, and lattice defects. By combining these techniques, this research can comprehensively understand the properties and behavior of hard carbon nanostructures, facilitating their optimization for various applications such as energy storage, catalysis, and nanoelectronics.

3.4.1 Scanning Electron Microscopy

Scanning electron microscopy (SEM) is a versatile technique for analyzing the microstructure and morphology of materials. In the 1890s, the discovery of electron deflection by a magnetic field led to the development of electron microscopy, which involved substituting the light source with a high-energy electron beam. This development entailed substituting the light source with a high-energy electron beam. [47, 48]

SEM samples are typically coated with a conductive layer such as carbon or a thin metal layer like gold to enhance electron conduction. Subsequently, the sample undergoes scanning by high-speed electrons that penetrate through the barrel. A detector quantifies the emitted electrons, reflecting the intensity of the sample area and generating three-dimensional shapes on a digital image. The resolution of scanning electron microscopes (SEM) ranges from 4 to 20 nanometers, depending on the particular model. [49]

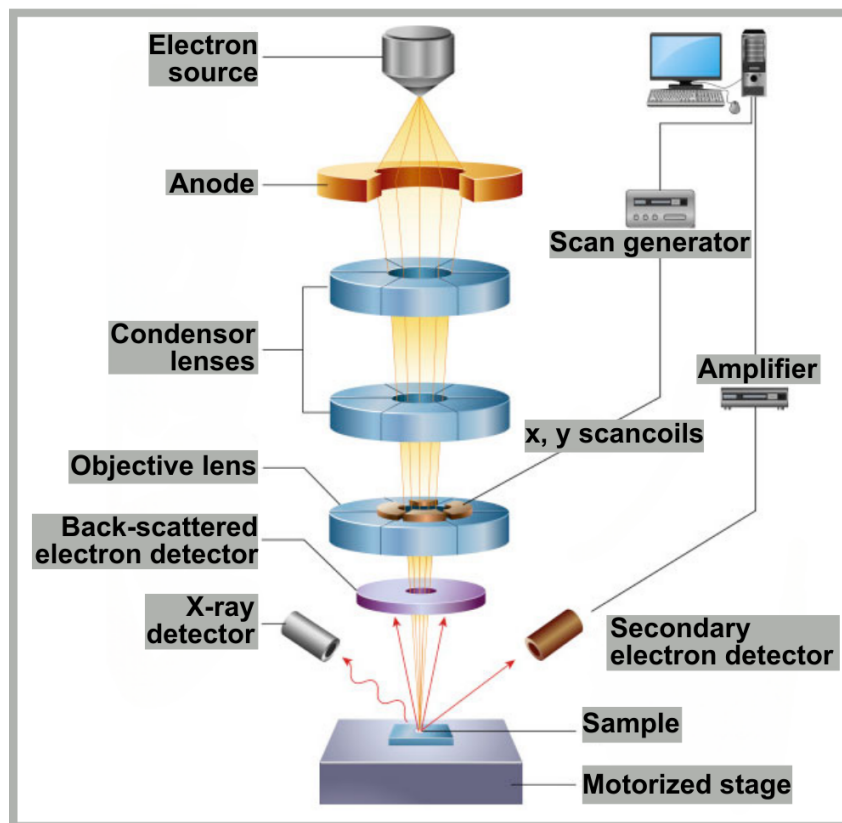


Figure 3.4: Scanning Electron Microscope working function.

SEM produces several signals, including secondary electrons, backscattered electrons, Auger electrons, characteristic x-rays, and photons with different energy levels. The most

used signals in SEM are the secondary electrons (SE) and backscattered electrons (BSE). These signals exhibit variations in the signal received due to differences in surface topography as the electron beam scans the specimen. Besides SEM, resolution refers to the minimum distance required to distinguish two points. Optical microscopes can enhance the resolution of the human eye (0.2 mm) by utilizing lenses or a combination of lenses. Despite continuous improvements in lens technology, the resolution of microscopy has been restricted not by the quality of the lenses but by the wavelength of the light source. The spectrum of white light spans wavelengths ranging from 400 to 700 nm , while electrons exhibit considerably shorter wavelengths, which results in enhanced resolution. The secondary electron (SE) emission is limited to a specific volume near the area where the electron beam impacts. This characteristic enables the acquisition of a relatively high resolution in the resulting image.

An electron gun generates a continuous flow of electrons, which are then accelerated by a voltage difference between the anode and the cathode. The acceleration voltage typically ranges from 0.1 keV to 50 keV , depending on the specific electron gun used. The electrons, moving at a high speed, possess significant kinetic energy. The condensing lens system and scanning coil guide the accelerated primary electrons to the sample, ensuring they have the smallest possible beam cross-section at the gun. This results in forming an electron probe with a $1 - 10\text{ nm}$ diameter and an electron-probe current ranging from 1×10^{-9} to $1 \times 10^{-12}\text{ A}$. As a result of the interactions between the electrons and the sample, the electrons slow down, and their energy is dispersed into various signals. The secondary electrons (SE) and backscattered electrons (BSE) are detected by a photomultiplier tube, which converts the electrons into an electrical signal. This signal is then amplified to generate an image.

The interaction may result in elastic or inelastic scattering when the accelerated electrons collide with the specimen. Elastic events impact the trajectory of the electron beam, but they do not cause any significant energy changes. In contrast, inelastic events result in energy transfer to the sample, which generates secondary electrons, Auger electrons, and x-rays. In the case of backscattered electron (BSE), a notable amount of the incoming beam scatters enough times to reverse its direction and exit the specimen completely. This process provides valuable data about the composition, mass thickness, and crystallography

of the specimen. The BSE signal exhibits a correlation with the atomic number, with an increasing trend as the atomic number increases. A slight correlation between the BSE signal and the beam current indicates a small energy dependence. Additionally, the tilt angle at which the beam strikes the sample will decrease the interaction volume, resulting in a tilt dependence. Adjusting the angle of the sample stage will result in an increase in the electron coefficient. Low-energy secondary electrons (SE) are formed when electrons with weakly bonded valence or conduction are ejected. As a result of their limited amount of kinetic energy, they will experience a rapid decline in energy as they travel a certain distance. The escape probability will exponentially decrease as the electron beam penetrates the sample. SE also exhibits a correlation with the atomic number, which is influenced by the number of electrons in the outer shell and the atomic radius. SE is particularly useful for revealing the morphology and topography of samples.

Finally, several factors will impact the final resolution of the SEM image: the current intensity, the final probe size, the electron optical system, and the electron optical column. One factor is the current intensity of the electron beam that strikes against the sample, which will determine the magnitude of the resulting signal. Additionally, the size of the final probe is a crucial factor that will determine the optimal scanning resolution. Then, the electron optical system is engineered to achieve the highest achievable current in the most compact electron probe. The components and design of the electron optical column may alter these factors.

3.4.2 Raman Spectroscopy

Raman spectroscopy analyzes the inelastically scattered light. In this technique, a small fraction of incident photons undergo inelastic scattering, known as Raman scattering, where the scattered light has a slightly different frequency than the incident light. This technique involves a two-photon inelastic light scattering event where the input photon, with higher energy than the vibrational quantum energy, transfers some energy to molecule vibration and scatters the remaining energy as a photon with reduced frequency. [50, 51] Raman spectroscopy offers a unique spectrum of distinct vibrations of a molecule, known as a "molecular fingerprint," which is useful for chemical identification.

Raman spectroscopy can offer insights into lower frequency modes and vibrations to

comprehend the crystal lattice and molecular structure of the spine. When light interacts with molecules in a gas, liquid, or solid, most photons disperse with the same energy as the original photons, a phenomenon known as elastic scattering or Rayleigh scattering; however, about one in ten million of these photons will undergo scattering at a frequency different from the original photon. [52] Organic molecules tend to glow more with shorter wavelength radiation; hence, wavelength monochromatic excitation sources such as solid-state laser diodes emitting light at 785 nm are commonly utilized. On the contrary, a shorter wavelength source, such as a 532 nm laser, is more accurate for inorganic molecules. [53]

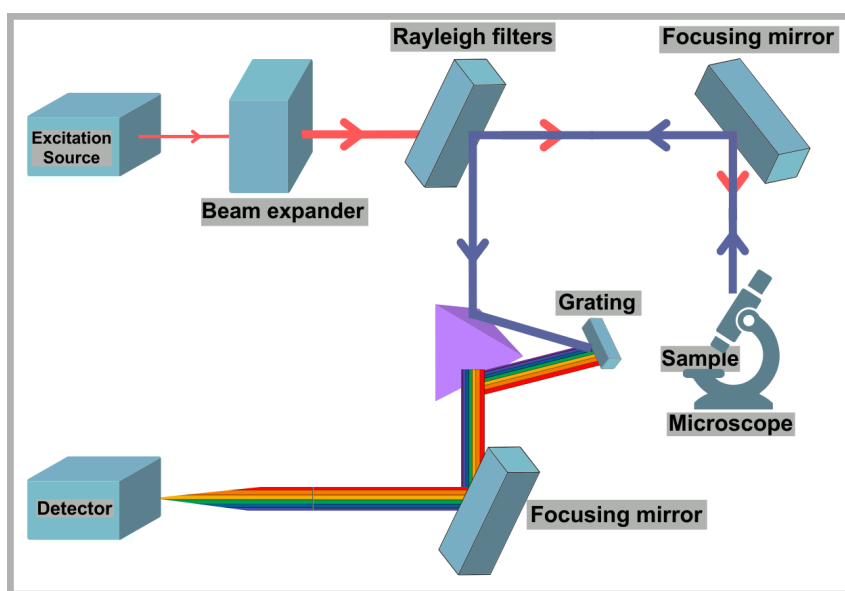


Figure 3.5: Raman Spectroscopy working function.

Introducing some concepts to complement the Raman Spectroscopy working principle is important. Then, light can interact with matter through three distinct mechanisms. Incident photons can absorb, scatter, or transmit (reflection) without interaction. Light scattering refers to the phenomenon of light being redirected when it encounters a solid, gas, or liquid material. This redirection occurs when an incident electromagnetic wave, such as monochromatic radiation, interacts with the material. When the incident electromagnetic wave interacts with matter, it creates a regular disturbance in the electron cloud of the molecules that comprise the material being analyzed. The perturbation will exhibit the identical frequency (ω_0) as the electric field of the incident wave. The charge within the molecules will periodically separate, resulting in the phenomenon known as induced

dipole moment. Scattered light is produced due to the oscillating-induced dipole moment, creating a new source of electromagnetic radiation. The scattering process can be classified as either elastic or inelastic, depending on the disparity between the spectra of the incident light and the scattered light. Elastic scattering refers to the phenomenon where the majority of radiation scattered by the irradiation of a monochromator is emitted at the same wavelength as the incoming laser radiation. Inelastic scattering refers to the phenomenon where incident light scatters at various wavelengths, resulting in a small amount of additional scattered light. Raman scattering is a form of inelastic scattering employed to identify molecules by offering chemical and structural information.

Scattering Types

Raman scattering describes how the incident photons interact with the material and the resulting energy changes. There are three primary types of scattering: Rayleigh scattering, Stokes scattering, and anti-Stokes scattering.

- Rayleigh scattering:

Rayleigh scattering occurs when incident photons scatter elastically off the material, meaning there is no change in the energy (or wavelength) of the photons. It has no energy change; the energy of the scattered photons is the same as that of the incident photons. Thus, it has no wavelength shift because the scattered light has the same wavelength as the incident light. Rayleigh scattering is the most common form of scattering and accounts for most scattered light. It provides limited information about the molecular vibrations of the materials since there is no energy transfer between the photons and the material.

- Stokes scattering:

Stokes scattering occurs when incident photons scatter inelastically, losing energy to the material. This energy loss corresponds to the excitation of vibrational modes in the material. The scattered photons have lower energy compared to the incident photons. The scattered light has a longer wavelength (lower frequency) than the incident light. Stokes scattering is of great importance in Raman spectroscopy. The energy difference between the incident and scattered photons corresponds to the

vibrational energy levels of the molecules in the material, providing a fingerprint that can be used to identify molecular structures and compositions.

- **Anti-Stokes scattering:**

Anti-Stokes scattering also involves inelastic scattering, but in this case, the incident photons gain energy from the material. This typically occurs when the material is already in an excited vibrational state, and the scattering process returns it to a lower energy state. The scattered photons have higher energy compared to the incident photons. The scattered light has a shorter wavelength (higher frequency) than the incident light. Anti-Stokes scattering is less intense than Stokes scattering because fewer molecules are excited at thermal equilibrium. However, the ratio of anti-Stokes to Stokes intensities can provide information about the temperature of the material, as the population of molecules in excited states follows a Boltzmann distribution.

Vibrational Modes

Raman spectroscopy is powerful for characterizing carbon materials such as graphite, graphene, diamond, and hard carbon nanostructures. The Raman spectra of these materials usually feature several prominent bands, notably the *D*, *G*, and *2D* bands. Each of these bands provides specific information about the carbon material, its structure, and its properties.

Raman spectroscopy is a crucial tool for analyzing and characterizing carbon-based materials. Raman Spectroscopy is a useful technique for analyzing hard carbon nanostructures. It can provide information about crystal size, chemical impurities, mass density, optical energy gap, elastic constants, doping, defects, and other forms of crystal disorder by the spectra the equipment provides after the measurements. A Raman spectrum is a graph that shows the intensities of the scattered light compared to the frequency shifts between the incident light and the scattered light. Different Raman scattering processes can be associated with various characteristics of carbon-based materials, such as hard carbon. These characteristics include the radial breathing mode (RBM), the *G band*, the *D band* induced by dispersive disorder, and its second-order harmonic, the *2D band*, also known as *G' band*.

- *D Band*

This band indicates disorder and defects in the carbon lattice. The location of this band is around 1350 cm^{-1} ; the exact position can vary depending on the excitation wavelength and the type of carbon material. The *D* band arises from the breathing modes of sp^2 atoms in rings and is associated with disorder and defects in the carbon structure. It is a non-degenerate total-symmetric vibration, which means it is symmetric under all symmetry operations (rotation, mirror plane, inversion center) that becomes active due to the presence of edges, grain boundaries, vacancies, or other defects in the otherwise perfect sp^2 carbon lattice. A higher *D* band intensity indicates more defects or disorders.

- *G Band* This band indicates the presence of sp^2 carbon atoms and provides information on structural integrity and electronic properties in carbon-based materials. The *G* band corresponds to the phonon at the Brillouin zone center due to the in-plane stretching vibrations of the sp^2 carbon atoms in the graphene lattice. It is a characteristic feature of graphitic materials. The *G* band is a primary indicator of the presence of sp^2 hybridized carbon atoms and provides information about the overall quality of the graphitic structure. Its position and shape can also give insights into strain, doping, and the number of layers in graphene.

- *2D band* It can be found around 2700 cm^{-1} . The *2D* band is the second-order overtone of the *D* band and does not require the presence of defects for activation. The *2D* band arises from a two-phonon double resonance process, which is sensitive to the electronic structure of the material. This band is particularly important for characterizing graphene. Its shape, sharpness, position, and intensity relative to the *G* band can reveal the number of graphene layers and the stacking order. In single-layer graphene, the *2D* band is typically sharp and intense, whereas in multi-layer graphene, it splits and becomes broader and less intense.

- *I_D/I_G Ratio*

The I_D/I_G is the ratio of the intensity of the *D band* (I_D) to the intensity of the *G band* (I_G) in the Raman spectrum. This ratio is highly important due to the information it gives, such as the disorder and defects, quality and crystallinity, and

how amorphous a material is, and allows a quantitative analysis. The I_D/I_G ratio is widely used to assess the level of disorder or the amount of defects in carbon materials. A higher I_D/I_G ratio indicates more defects or a higher degree of disorder in the material. This is because the *D band* is defect-activated, increasing its intensity with the number of defects. Conversely, a lower I_D/I_G ratio suggests fewer defects and higher crystallinity. The *D band* is weak or absent in highly crystalline graphite or high-quality graphene, resulting in a low I_D/I_G ratio. On the other hand, in amorphous carbon materials, where there is a significant amount of disorder, the I_D/I_G ratio tends to be high.

3.4.3 X-ray Photoelectron Spectroscopy

X-ray photoelectron spectroscopy (XPS) is ideal for analyzing surface chemistry and is proven to be an effective tool for studying the chemical composition of materials. It can be utilized to analyze tribo-boundary films through various methods such as survey scanning, element mapping, detecting binding energy shifts, and creating composition depth profiles. By combining XPS with electron microscopies, detailed microstructural and chemical data of the tribo-boundary film can be acquired to understand material and lubricant interactions in a wear process. [54] X-ray photoelectron spectroscopy (XPS), or ESCA, is a technique that examines the energy distribution of electrons emitted from compounds exposed to X-ray radiation. This method is utilized to analyze the surface composition of a material, offering qualitative and quantitative data, and can identify the chemical state of the elements within. This method is suitable for examining surfaces and boundaries. [54]

To understand its working principle, it is important to learn that X-ray Photoelectron Spectroscopy (XPS) is a precise spectroscopic technique that quantitatively measures the elemental composition, empirical formula, chemical state, and electronic state of the elements on the surface of a material. The working principle of XPS is ruled by a three-step process, which includes X-ray excitation, Photoelectron emission, and detection and analysis. [55]

- 1. X-ray excitation

During the initial stage, the material sample undergoes irradiation with monochro-

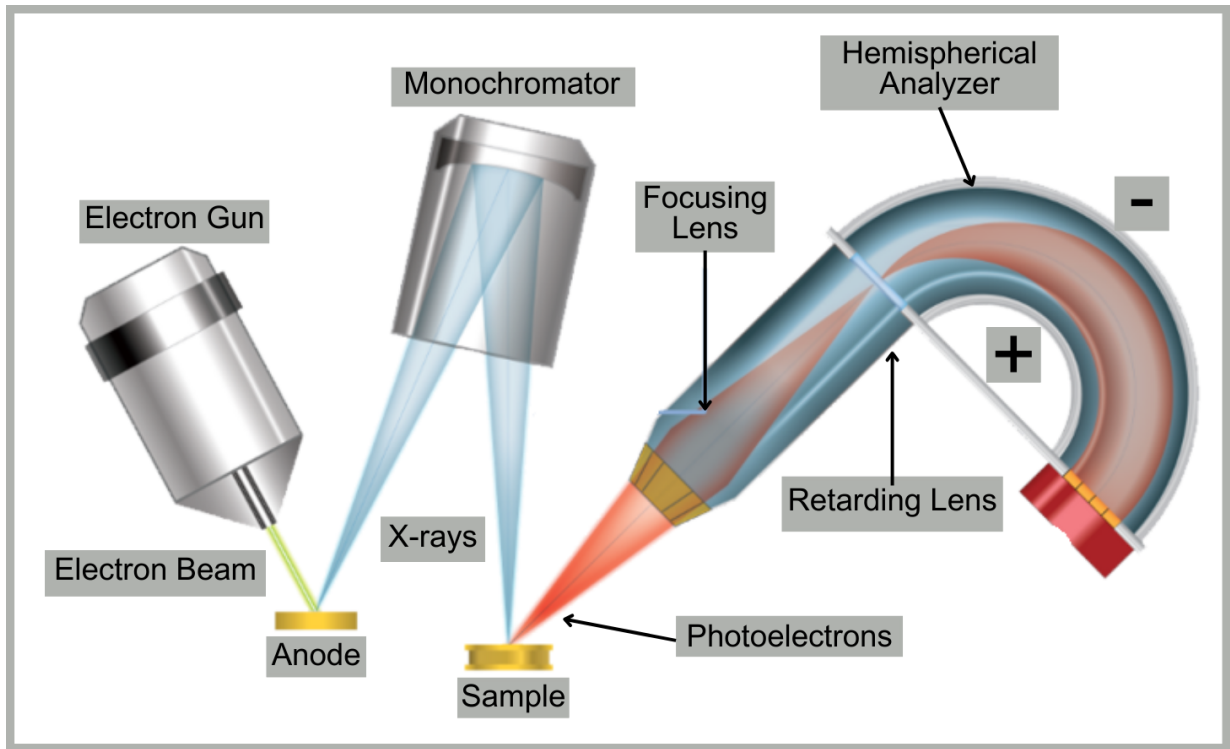


Figure 3.6: X-Ray Photoelectron Spectroscopy working function.

matic X-rays, which are typically produced by sources such as aluminum ($Al K_{\alpha}$) or magnesium ($Mg K_{\alpha}$) anodes. The energy of the incident X-rays ($h\nu$) is high enough to cause ionization of atoms in the material by ejecting core-level electrons. The photoelectric effect explains this process, in which an atom absorbs an incident photon, resulting in the emission of a photoelectron.

- 2. Photoelectron emission

The photoelectron, ejected from the core level of an atom in the sample, possesses a measurable kinetic energy (KE). The equation $KE = h\nu - BE - \gamma$ provides the value for the kinetic energy of the released photoelectron. Where $h\nu$ is the energy of the incident X-ray photon, BE is the binding energy of the electron in its initial state within the atom, and γ is the work function of the spectrometer (a correction factor accounting for the energy required to move an electron from the sample surface into the vacuum of the spectrometer). The binding energy can be determined by measuring the kinetic energy ejected electrons since $h\nu$ and γ are known quantities.

- 3. Detection and analysis

In the final stage, the emitted photoelectrons are detected and subsequently analyzed. The XPS instrument collects the electrons that escape from the surface (typically from a depth of 1-10 nm) and categorizes them by their kinetic energy using an electron energy analyzer. This results in spectra that plot the number of detected electrons (intensity in the Y axis) against their binding energy. The resulting spectrum consists of peaks corresponding to the binding energies of electrons in different atomic orbitals. These peaks provide information about elemental composition (the position of the peaks determines the elements present in the sample), chemical state (shifts in the binding energy peaks can indicate the chemical state or oxidation state of the elements), and quantitative analysis (the area under each peak is proportional to the concentration of the corresponding element in the sample).

In XPS, the data collected can be broadly categorized into survey spectra and high-resolution spectra. Each type of spectrum serves a different purpose in the analysis of the sample, providing complementary information about the surface of the material composition and chemical states.

The survey spectrum (also known as a wide scan or overview spectrum) provides a broad overview of the elements present on the surface of the sample. It covers a wide range of binding energies, typically from 0 to 1200 eV, depending on the X-ray source and the material being analyzed. It allows for detecting all elements (except hydrogen and helium, which XPS cannot detect) present on the surface within the probing depth of the technique, which is typically 1 – 10 nm. The survey scan encompasses a wide range of binding energies, ensuring that peaks from all elements on the surface are captured. Peaks corresponding to the core levels of different elements are identified based on their binding energies; as each element has characteristic binding energies, it is possible to determine which elements are present. In a survey spectrum, there might be peaks corresponding to carbon ($C1s$), oxygen ($O1s$), nitrogen ($N1s$), and other elements depending on the sample. This provides a qualitative and semi-quantitative overview of the surface composition.

On the other hand, high-resolution spectra focus on a narrow binding energy range around the core levels of specific elements identified in the survey scan. These spectra provide detailed information about the chemical states of the elements. The primary pur-

pose of high-resolution spectra is to investigate the chemical states (or oxidation states) and the electronic environment of specific elements. This detailed analysis helps in understanding the bonding and chemical composition of the surface at a much finer level. The position and shape of the peaks can indicate the oxidation state and chemical bonding of the element. For example, the C 1s peak can show different components corresponding to different carbon-oxygen bonds ($C - C$, $C - O$, $C = O$).

3.4.4 X-Ray Diffraction

X-ray diffraction (XRD) is a non-destructive method that offers in-depth data on the crystallographic structure, chemical composition, and physical characteristics of materials. It can also accurately determine lattice parameters, tension, crystalline sizes, and preferential orientation. X-ray diffraction in a polycrystalline sample can identify crystalline phases based on their characteristic diffractogram, both qualitatively and quantitatively. This technique is typically used to study polymorphism, phase transitions, solid solutions, measurement of particle size, and determining phase diagrams. XRD peaks result from the constructive interference of a monochromatic X-ray beam scattered at specific angles by each set of lattice planes in a sample. The atomic positions influence peak intensities in the lattice planes. [56]

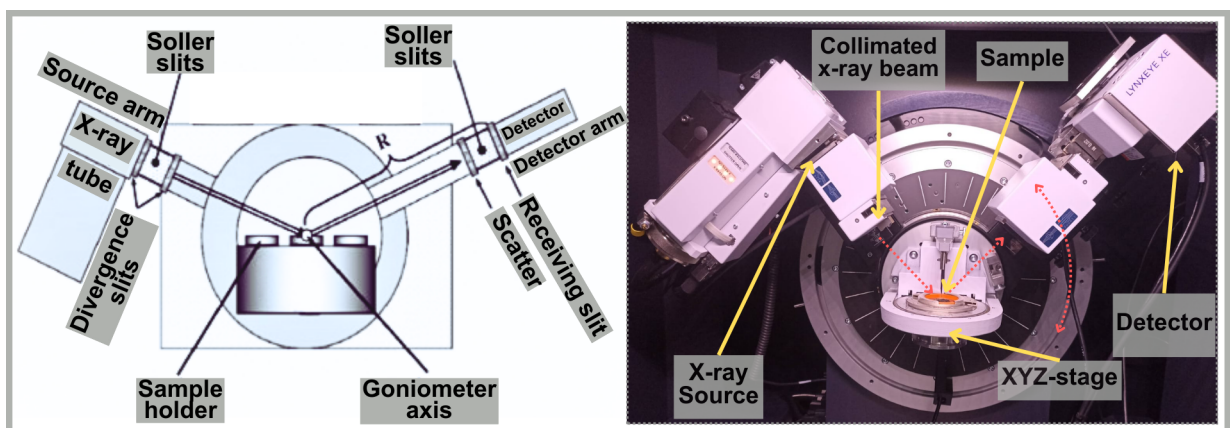


Figure 3.7: X-Ray Diffraction working function.

Besides, Bragg's Law is a fundamental principle used in X-ray diffraction (XRD) to relate the angles at which X-rays are diffracted by the atomic planes in a crystalline material to the distance between those planes. This relationship is critical for determining the crystal

structure of materials.

When X-rays are incident on a crystalline material, they are scattered by the electrons in the crystal atoms. In a crystal, the atoms are arranged in regular, repeating planes. When the X-rays encounter these planes, constructive interference occurs at specific angles, leading to distinct diffraction peaks. Bragg's Law describes the condition for this constructive interference. For constructive interference to occur (i.e., for the diffracted X-rays to be in phase and produce a detectable signal), the path difference between the X-rays scattered from successive atomic planes must be an integer multiple of the wavelength of the X-rays. This condition can be visualized by considering the geometry of the incident and scattered X-rays and the crystal planes.

Bragg's Law is mathematically expressed as $n\lambda = 2d\sin\theta$. Where n is an integer (the order of the diffraction peak), d is the distance between the atomic planes in the crystal (also known as the interplanar spacing), λ is the wavelength of the incident X-rays, and θ is the angle between the incident X-ray beam and the crystal plane (known as the Bragg angle).

3.4.5 Transmission Electron Microscopy

Transmission Electron Microscopy (TEM) is a powerful microscopy method that analyzes the material structure, morphology, and composition at the nanoscale. TEM involves passing a focused beam of electrons through a thin sample, where interactions with the atoms generate an image based on electron scattering and absorption. Transmission electron microscopy (TEM) uses a concentrated electron beam generated by an electron source, usually a tungsten filament or a field emission gun (FEG). The electrons are accelerated to high energies, usually ranging from tens to hundreds of kilovolts, and then focused into a narrow beam with electromagnetic lenses. TEM samples need to be thinly sliced (usually less than 100 nanometers thick) to enable electron transmission. This is commonly accomplished using ultramicrotomy for biological samples or focused ion beam (FIB) milling for solid materials. Subsequently, the slender sections are affixed to a Transmission Electron Microscope (TEM) grid, consisting of a thin backing material (typically carbon or copper) with evenly distributed perforations. When the electron beam interacts with the atoms in the specimen, it leads to phenomena like elastic scattering, inelastic scattering, and

absorption. The interactions result in an intricate pattern of transmitted electrons that contain details regarding the structure and composition of the specimen. Electrons sent out are gathered by a detector, like a fluorescent screen or a charge-coupled device (CCD) camera, to create an image. High-resolution images of the specimen's internal structure can be obtained by analyzing the intensity and angle of the transmitted electrons. Transmission electron microscopy (TEM) can achieve exceptional resolution, reaching atomic scales, thanks to the short wavelength of electrons. Contrast in TEM images results from differences in electron scattering within the specimen, revealing details like crystal defects, grain boundaries, and chemical composition. [57, 58]

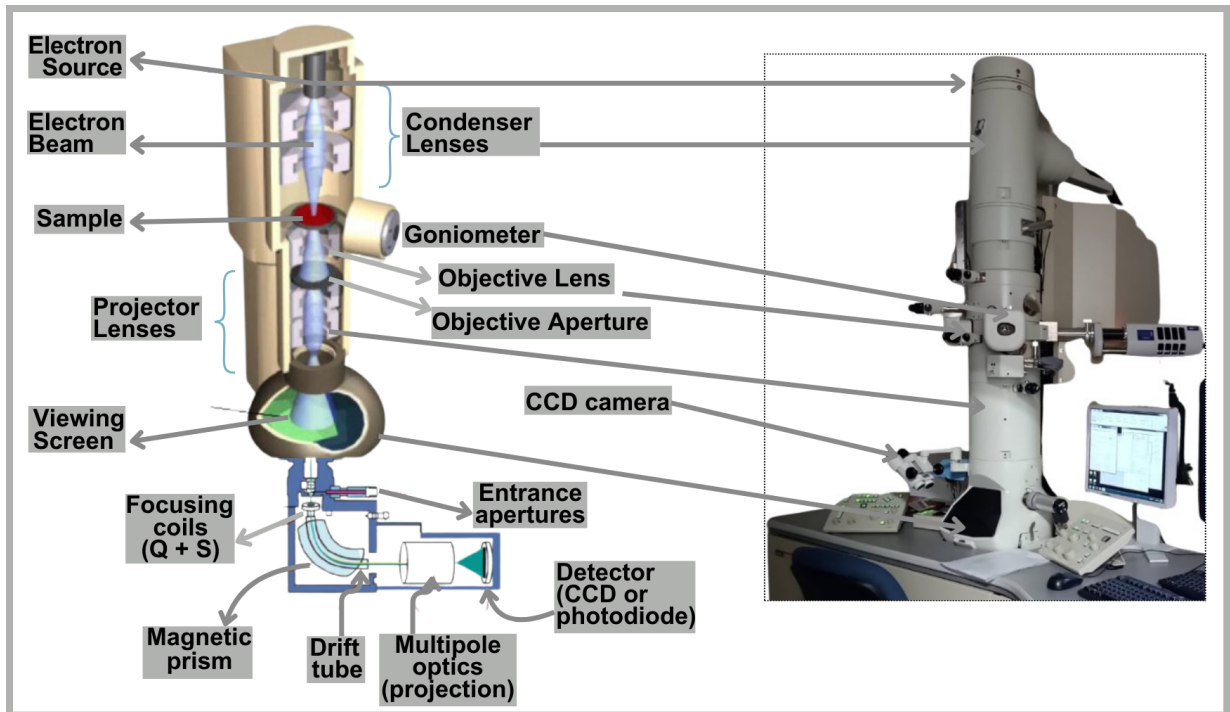


Figure 3.8: Transmission Electron Microscopy working function.

Chapter 4

Methodology

This section describes the experimental procedure of the investigation, which consists of sample preparation and synthesis. It also describes the parameters and details of the characterization techniques used to analyze the material change.

4.1 Sample Preparation

The sample preparation objective was to prepare flat-surface pills only using physical treatments for the laser treatment. So, the sample preparation consisted of collecting the target raw material, drying, ball milling, sieving, and pill making, as shown in Figure 4.1.

For the first step in this research, it was considered *Parajubaea Cocoides*, an Ecuadorian native palm species, as the raw material. [44] Then, two fruits of *Parajubaea Cocoides* palm (two dwarf coconuts) were collected at Yachay Tech University. The coconut section of interest was only the exterior fibrous shell, as seen in the first step of Figure 4.1; thus, the shell was extracted by hand, using gloves in a sterilized environment, to avoid damaging or contaminating the sample, as seen in the image.

In the second step, the coconut shell was left to dry for 72 hours in the oven at $60\text{ }^{\circ}\text{C}$. The equipment from the School of Physical Sciences and Nanotechnology Laboratory at Yachay Tech University was used. After this process, the first sample of interest, the pristine sample (sample *A*), was obtained.

The dried coconut shell was then taken into the ball milling as the third step in the sample preparation process, as seen in Figure 4.1. The dried coconut shell was ball milled with a frequency of 6 Hz for three hours, with a milling sphere of 2 cm in diameter. The



Figure 4.1: Graphical methodology of Sample Preparation.

remaining milled material was sieved and separated into two different samples differentiated by particle size. Following the fourth and fifth steps seen in Figure 4.1. Thus, taking place the next two samples of interest are the $A1T$ sample and the $A1T75$ sample. The difference between the last two mentioned is that sample $A1T$ has a particle size bigger than $75\ \mu\text{m}$, and sample $A1T75$ has a particle size between $45\ \mu\text{m}$ and $75\ \mu\text{m}$, as shown in Table 4.1. Two different sieves were used ($45\ \mu\text{m}$ and $75\ \mu\text{m}$). However, the material remaining under $45\ \mu\text{m}$ was not considered because of its inconsiderable amount.

Sample Name	Description
A	Pristine Sample
$A1T$	Particle size: $75\ \mu\text{m} < A1T$
$A1T75$	Particle size: $45\ \mu\text{m} < A1T75 < 75\ \mu\text{m}$

Table 4.1: Description of the particle size of samples used.

The final sample preparation step was pill making, using the mechanical press adapted in the Laboratory of the School of Physical Sciences and Nanotechnology at Yachay Tech University. See Figure 4.1 step 6, in which a mechanical press, with a pill in between the arms of the press, is represented. Different conditions were employed in the mechanical press for sample $A1T$ and sample $A1T75$. In the case of sample $A1T$, a pressure of $25\ \text{MPa}$

was applied with a relaxation time of one minute, and for sample *A1T75*, a pressure of 5 MPa was used to make the pills. The dimensions of the pills were standard; they had a diameter of 9 mm, a height of 4 mm, and a weight of 0.15 g, see Figure 4.1 step 6, where a photograph of the final pill is presented.

4.2 Synthesis of the Hard Carbon Nanostructures

The synthesis method used in this research was laser ablation, a procedure derived from pyrolysis, which consists of applying controlled heat to eliminate the biomass of organic compounds while reorganizing the carbonous structures at the atomic level. It used a FORZA6-80W industrial laser cutter. As its name indicates, the maximum power of the laser cutter is 80 W. The parameters such as intensity, working distance, area of irradiation, and laser velocity were strictly controlled only to affect the surface of the pills. To better understand, see Figure 4.2.

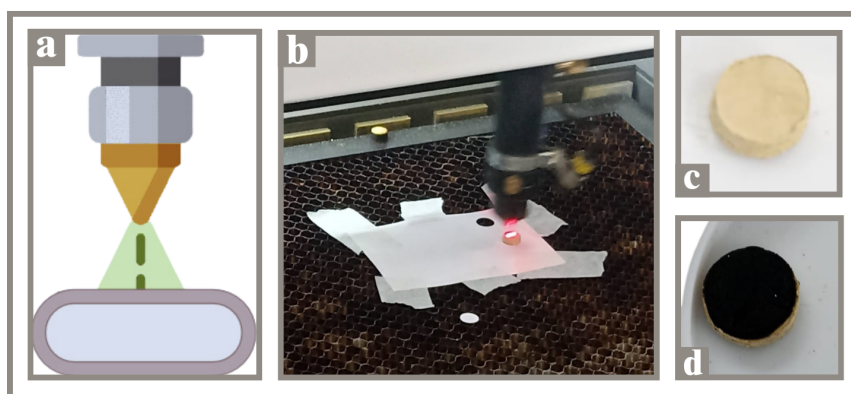


Figure 4.2: Synthesis method used: laser ablation. a. Schematic representation of the laser beam irradiating the sample pill. b. Image taken of the laser ablation synthesis, carried out in the Physics Laboratory at Yachay Tech University. c. Pristine sample *A1T75*. d. Synthesized sample *A1T75*.

Image a of the Figure 4.2 shows a schematic representation of the synthesis process, which shows the laser source irradiating only the surface of the pill. Image b is the Image taken of the synthesis carried out in the laboratory at Yachay Tech University. It shows the laser source irradiating the *A1T75* sample pill in the work cabin of the *FORZA6 – 80W* laser cutter. Image c is the pristine pill taken from sample *A1T*, and image d is the synthesized sample pill with the obtained material on the top of the pill of the sample *A1T*

after the laser irradiation shown in image b.

The parameters used for the synthesis process were controlled and specific. In the case of the laser intensity, the range used was between 7 % as the minimum power and 9 % as the maximum power, and the velocity of the laser was 100 *nm/s* with an interline space of 0.02 *mm*. The working distance of the laser is standardized because of the laser focus, which is equal to 10.65 *mm*, and the speed of the laser was 50 *nm/s*. The laser irradiated the whole surface area of the pills to have a better approach to the material. See figure c of Figure 4.2.

4.3 Characterization Techniques

Five different characterization techniques were employed to demonstrate the synthesis of hard carbon nanostructures: Scanning Electron Microscopy (SEM), Raman Spectroscopy, X-ray Photoelectron Spectroscopy (XPS), X-ray Diffraction (XRD), and Transmission Electron Microscopy (TEM).

4.3.1 Scanning Electron Microscopy

Scanning Electron Microscopy (SEM) measurements were carried out in two stages of the investigation. The first SEM measurement took place at the very beginning of the investigation to provide a guide on the composition of the raw material. It was developed with a scanning electron microscope, model Phenom ProX G6 Desktop SEM X with an integrated Energy-Dispersive X-ray Spectroscopy (EDS) detector (as seen in Figure 4.3). The second SEM approach was carried out in the School of Physical Sciences and Nanotechnology Characterization Laboratory, and the scanning electron microscope integrated into the photoelectron spectrometer equipment was used.

The importance of using two different SEM approaches is that the first approach analyzes the structure of the pristine material to guide and give direction to the research while taking advantage of the integrated EDS for analyzing the chemical atomic composition of the pristine sample. This gave the initial idea of the presence of lignin, starch, and cellulose in the precursor material, or pristine sample, *A*. On the other hand, taking the SEM with the integrated equipment to the XPS, was crucial for having the different characterizations

of the sample samples. Also, it was highly important to obtain the SEM images of the three different samples: *A*, *A1T*, and *A1T75*. Finally, the information obtained from SEM, EDS, and XPS will permit the researchers to conclude which is the composition of the pristine sample and how it changed to obtain the synthesized hard carbon nanostructures.

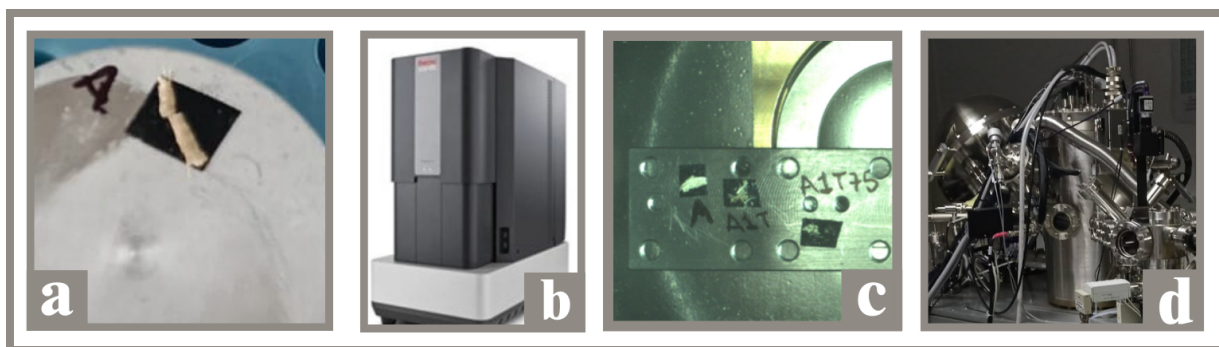


Figure 4.3: Scanning Electron Microscopes used. a. Sample prepared for first approach SEM measurement. b. Scanning electron microscope model Phenom ProX G6 Desktop SEM X. c. XPS sample holder with samples pristine *A*, synthesized *A1T*, and *A1T75*. d. Scanning electron microscope integrated into the photoelectron spectrometer.

The protocol was as clean as possible for the sample preparation to avoid contamination; thus, a small amount of pristine sample, *A*, was placed on an SEM pin and attached to it with carbon tape, see image a of Figure 4.3. The acceleration voltage used for taking the SEM images was 5 *kV*, and for the EDS measurement, the accelerating voltage reached 10 *kV*.

In the second approach, the scanning electron microscope integrated into the X-ray photoelectron spectrometer was used at the Characterization Laboratory of the School of Physical Sciences and Nanotechnology at Yachay Tech University. To prepare the samples, they were placed carefully in an XPS sample holder, and carbon tape was used to attach them to the holder, see image f of Figure 4.3.

4.3.2 Raman Spectroscopy

A Horiba LabRAM HR Evolution spectrometer was used at the Characterization Laboratory of the School of Physical Sciences and Nanotechnology at Yachay Tech University to obtain the Raman spectra, as shown in Figure 4.4. For the sample preparation, a piece of coconut fiber was placed on a glass slide for the pristine sample characterization, sample

A. In the case of synthesized samples $A1T$ and $A1T75$, as the hard carbon nanostructures were part of the pill surface, the complete pills were placed on the glass slide one by one, as seen in image e of Figure 4.4. The glass slide was carefully cleaned and purified before placing each sample on it to prevent contamination from disturbing the samples and affecting the results. The Raman spectra were collected by exciting the samples with the 532 nm laser wavelength source and the $x20_VISFLN$ objective for the synthesized samples, $A1T$ and $A1T75$. In the case of the pristine sample A , the Raman spectra were collected by exciting the sample with the 532 nm and the 785 nm laser wavelength source, with the $x20_VISFLN$ objective.

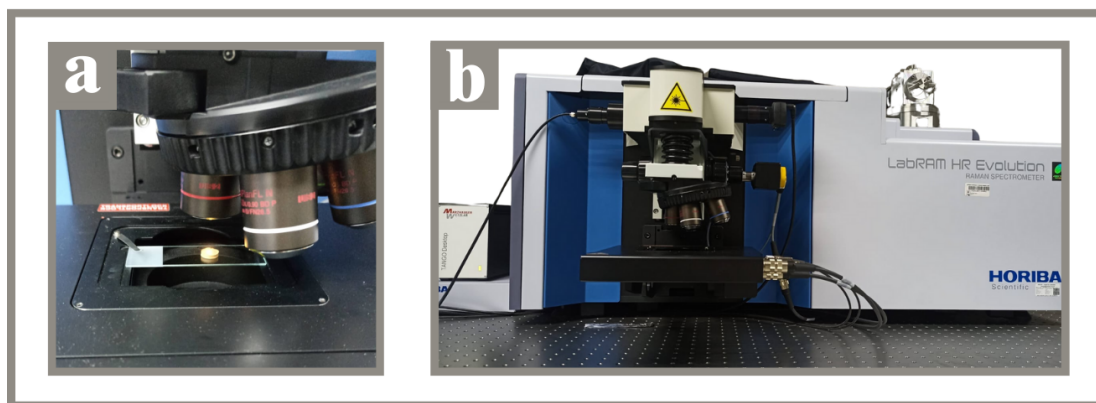


Figure 4.4: a. Raman Spectrometer with pristine sample $A1T75$. b. Horiba LabRAM HR Evolution spectrometer from Characterization Laboratory at Yachay Tech University.

4.3.3 X-Ray Photoelectron Spectroscopy

The VersaProbe III 5000 photoelectron spectrometer was used at the Characterization Laboratory of the School of Physical Sciences and Nanotechnology at Yachay Tech University to obtain the X-ray photoelectron spectroscopy (XPS) measurement; see Figure 4.5. The measurements were performed with the $Al K_{\alpha}$ X-rays with a photon source energy of 1486 eV in a high vacuum environment. To prepare the samples, they were placed carefully in an XPS sample holder, and carbon tape was used to attach them to the holder, as seen in image f of Figure 4.5. As XPS is the exact equipment for detecting any element or compound that might contaminate samples, the holder and the instruments used to prepare the samples were carefully cleaned and purified, and the sample preparation was carried out in a clean environment. A survey and high-resolution scans of the elements of

interest $C1s$, $N1s$, and $O1s$ were collected for each sample.

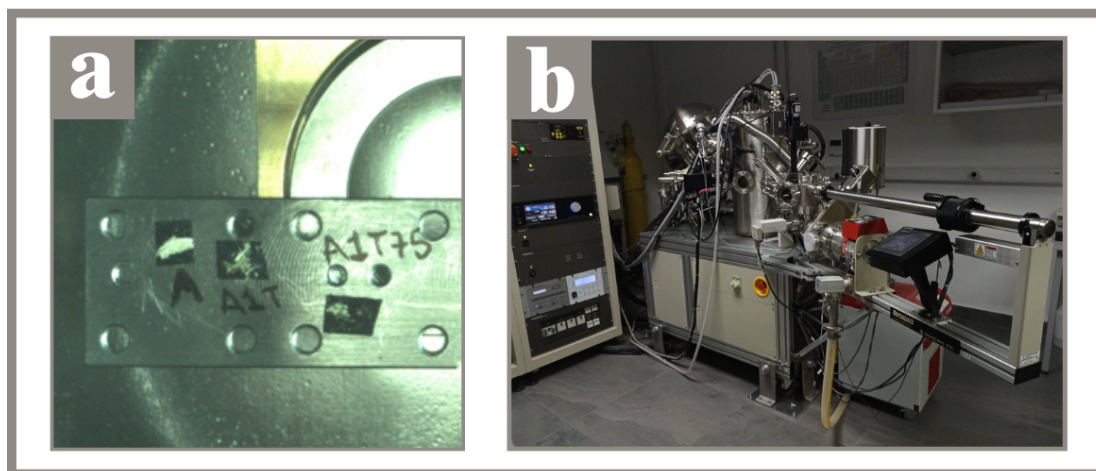


Figure 4.5: a. XPS holder was prepared with samples of pristine A , synthesized $A1T$, and $A1T75$. b. VersaProbe III 5000 photoelectron spectrometer from Characterization Laboratory at Yachay Tech University.

4.3.4 X-Ray Diffraction

The XRD analysis was conducted in the Physics Laboratory at "Universidad San Francisco de Quito" (USFQ). The equipment employed was an X-ray diffractometer D8 ADVANCE by Bruker to measure the samples. See image b of Figure 4.6.

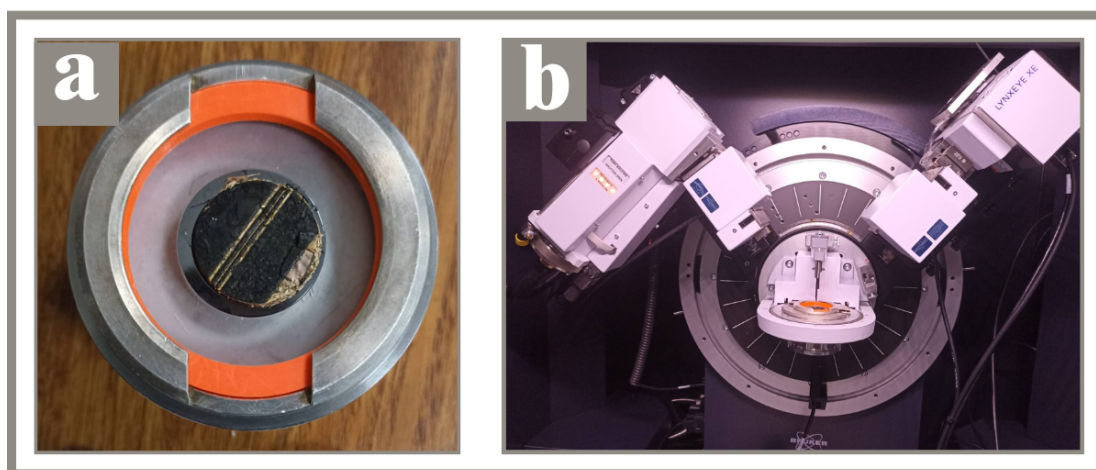


Figure 4.6: a. XRD holder prepared with $A1T$ sample. b. X-ray diffractometer D8 ADVANCE by Bruker from Physics Laboratory at USFQ.

For the XRD measurements, they were prepared different size pills with the same preparation conditions (pressure of 25 MPa for $A1T$, 5 MPa for $A1T75$) as well as with

the same synthesis conditions (laser intensity of 7 – 9 %) due to the sample holder size, see image a of Figure 4.6. The samples were prepared in a clean and purified environment to avoid contaminating them; the sample holder was well-sanitized before each measurement.

4.3.5 Transmission Electron Microscopy

The Transmission Electron Microscope measurements were carried out in the "Centro de Investigación en Ciencias de la Salud y Biomedicina" (CICSaB) at "Universidad Autónoma de San Luis Potosí" (UASLP), Mexico. The equipment model used was the Jeol Electron Microscope 2100 (JEM-2100), a 200 *kV* analytical electron microscope, see Figure 4.7.

The sample preparation was developed carefully in a clean and sanitized environment. A small amount of each sample was put in different ependors; then, 1.5 *ml* of distilled water was used to disperse the material, and a bath sonication process of 30 *minutes* was performed. Finally, 10 *uL* of each solution was deposited in full-carbon gratings and let dry completely at room temperature, as seen in image h of Figure 4.7. The measurements were taken only in bright fields, and High-Resolution TEM was achieved to analyze the semi-crystalline nanostructure of hard carbon.

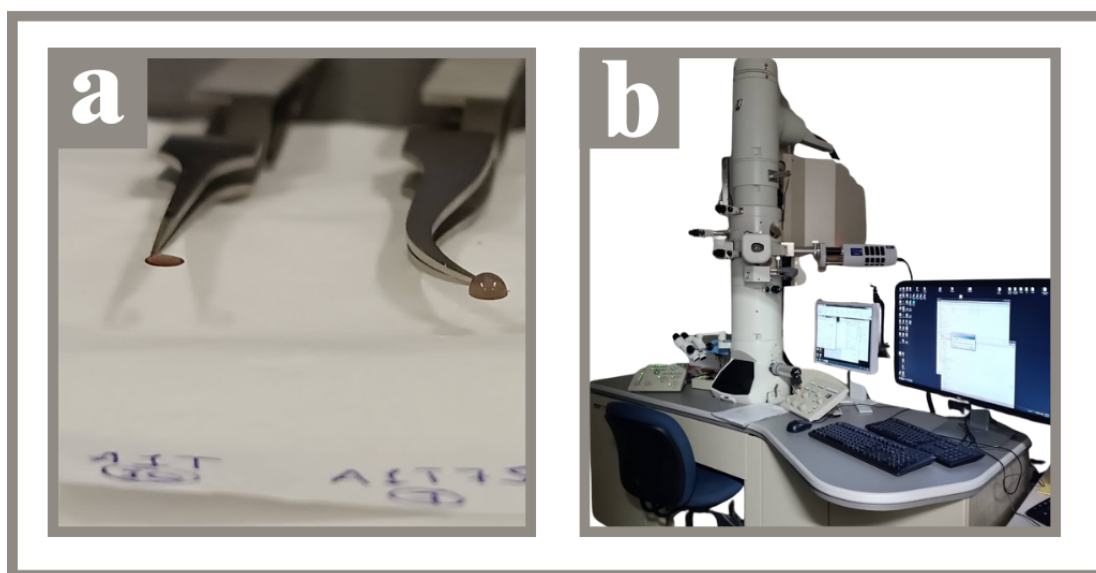


Figure 4.7: a. Sample preparation for TEM measurements of synthesized samples A1T and A1T75 in full-carbon gratings. b. Jeol Electron Microscope 2100 (JEM-2100) from CICSaB Laboratory at UASLP, Mexico.

Chapter 5

Results and Discussion

The corresponding characterization analysis and its representation of data will be presented in the forthcoming chapter. For a better understanding, the scanning electron microscopy (SEM) images are presented to show a macroscopic view of the material, both pre-synthesis and post-synthesis, facilitating a visual comparison. Subsequently, Raman spectra will be discussed to clarify the structural characteristics of the carbonaceous material acquired through synthesis. The x-ray photoelectron spectroscopy (XPS) analysis results will be presented to explain the chemical bonding configurations within the pristine and synthesized samples. To complement the last mentioned information, x-ray diffraction (XRD) analysis is presented to assess the crystallinity of the nanostructure. To finally complement these analyses, transmission electron microscopy (TEM) images will be integrated to understand the morphology and nanostructural characteristics, helping determine whether the synthesized material aligns with the expected hard carbon nanostructures.

5.1 Samples

It has to be mentioned again the differences between each sample. Thus, as seen in Figure 5.1., two images seem to be the same, but it is incorrect. In Figure 5.1, image a, sample *A* can be observed, the pristine sample, which directly corresponds to the *Parajubaea Cocoides* shell or husk. This pristine sample was characterized in the different stages of the research after the drying procedure. Then, image b of Figure 5.1 represents the material before the synthesis process, after the ball milling and sieving. There were two types of these pills differentiated by their particle size. The first particle size corresponded to be

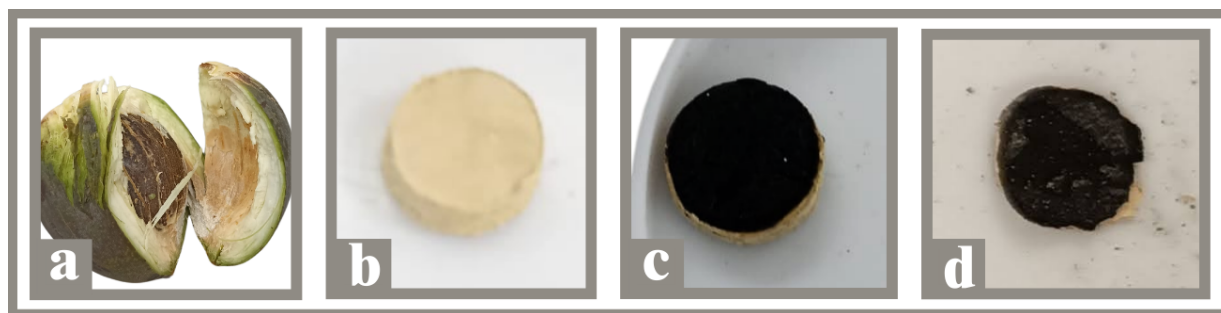


Figure 5.1: Images of samples at different stages of the research. a. Pristine sample, A. b. Pill sample with particle size between $45\ \mu\text{m}$ and $75\ \mu\text{m}$. c. A1T synthesized sample. d. A1T74 synthesized sample.

bigger than $75\ \mu\text{m}$, and the second particle size corresponded to a range between $45\ \mu\text{m}$ and $75\ \mu\text{m}$. About the images c and d of Figure 5.1., those correspond to the samples after the synthesis process; the c image is the sample A1T, which corresponds to the particle size A1T, being $>75\ \mu\text{m}$; the image d, corresponds to the sample A1T75, the synthesized sample with a particle size between $45\ \mu\text{m}$ and $75\ \mu\text{m}$.



Figure 5.2: Images of samples before, during, and after the synthesis process. a. Samples before the laser ablation process, image taken in the laser cutter cabin. b. XPS sample holder with the samples prepared before the measurements. c. Image of synthesized samples A1T and A1T75 after the surface scraping. d. Mechanical press stage where pills were prepared, and samples on its containers.,

The Figure 5.2 represents the number of samples produced and characterized in this research. Thirty different pills were produced corresponding to fifteen samples of sample A1T, with a particle size bigger than $75\ \mu\text{m}$, and fifteen samples of A1T75 with a particle

size of $45\ \mu\text{m}$ and $75\ \mu\text{m}$. Image a of Figure 5.2 corresponds to the samples before the laser ablation process in the laser cutter cabin. Image b corresponds to the pills in the XPS holder, a sample preparation process for their characterization. Image c corresponds to the sample preparation for TEM characterization in its initial stage; the surface of the pills was scraped carefully to obtain the darkest material; however, the A1T75 sample broke, showing to be fragile. Finally, image d of Figure 5.2 corresponds to the sample preparation stage in the mechanical press equipment at the Laboratory in Yachay Tech; in this image can be appreciated a notion amount of samples prepared for being studied in the research.

5.2 Scanning Electron Microscope

As presented before, Scanning Electron Microscope (SEM) images were taken at different stages of the investigation in different laboratories. Starting from the images taken at Conocoto Laboratory with the ProX G6 Desktop SEM X with an integrated Energy-Dispersive X-ray Spectroscopy (EDS) detector. In Figure 5.1., there are presented two SEM images of the pristine sample A, which corresponds to the *Parajubaea Cocoides* coconut shell, at two different magnifications. The material can be appreciated generally in image a. of the Figure 5.3., there can be distinguished a periodical structure conformed by granules and fibers. In image b., the coconut shell structure can be better appreciated in detail. In image b, these two main elements mentioned, the fiber structures and the granules, can be better appreciated for a periodical distribution. Adding to it in image b of the Figure 5.3., there can be appreciated zones encapsulated by fibbers, more specifically, periodical zones enclosed by dwarf coconut fibbers containing granules on their inside.

As the first stage of this research was to characterize *Parajubaea Cocoides*, the pristine sample, recognizing the structure by its physical characteristics is the first approach, as there is no literature review about it to date of *Parajubaea Cocoides* species. Interestingly, there are no reports of granules in conventional coconut shell (*cocos nucifera*) structures; however, compared with studies in different materials, having granules in biomaterials usually corresponds to a starch composition. However, there is a close species to *Parajubaea Cocoides* that is the *Babassu Coconut* species; according to Barrera et al., in the *Babassu coconut* species, there is a $23\ \text{wt}\%$ of starch in its composition. [59] Because the *Babassu*

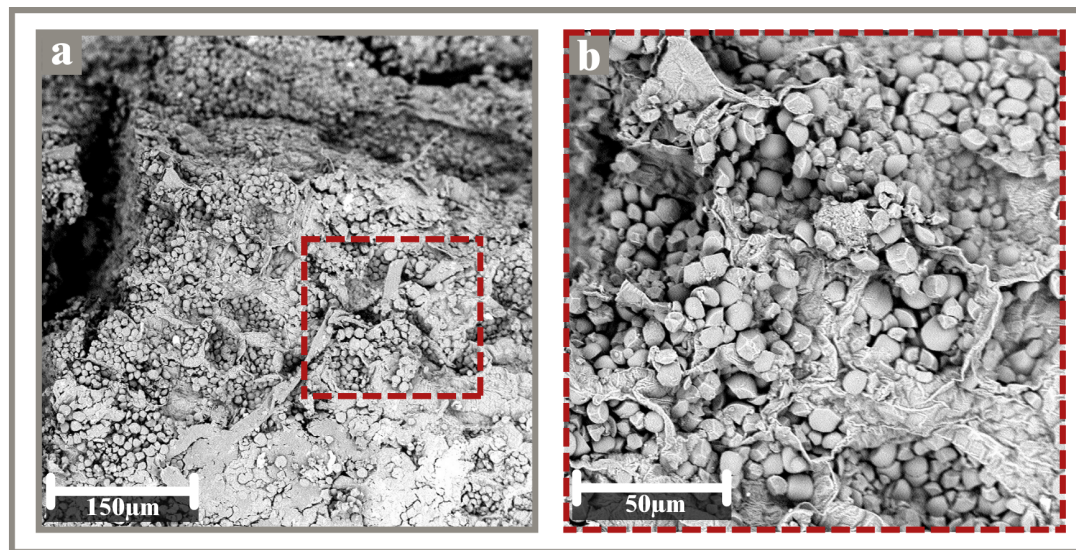


Figure 5.3: Images obtained with Phemom ProX G6 Desktop SEM X. a. Image taken at 500X magnification, total height 497 μm , and accelerating voltage of 5 kV. b. Image taken at 1700X magnification, with a total height of 158 μm and an accelerating voltage of 5 kV.

coconut species corresponds to the same family as the *Parajubaea Cocoides* family, *Areaceae*, the granules present in Figure 5.3. can be assigned to be starch granules. [60] It has also been reported that the coconut shell of *Cocos Nucifera* species contains fibers that correspond to a high composition of lignin and cellulose, according to Amara et al. *Parajubaea Cocoides* is categorized in the same family as *Cocos Nucifera*, and the fibers contained in *Parajubaea Cocoides* can be assigned to a material containing lignin and cellulose. [61, 18]

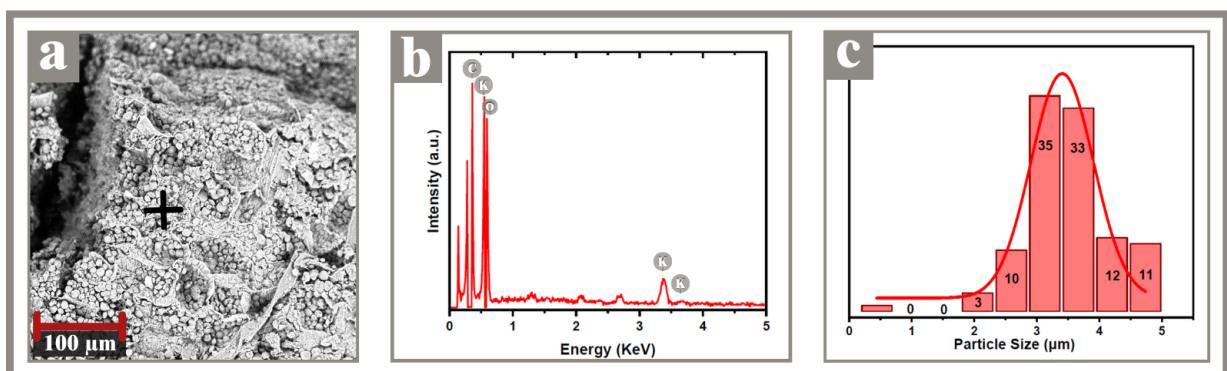


Figure 5.4: EDS obtained with Phemom ProX G6 Desktop SEM X. a. SEM image with the EDS point: The image was taken at 750X magnification, with a total height of 358 μm and an accelerating voltage of 10kV. b. EDS spectra. c. Particle size distribution of starch on image a.

Element	Atomic Percentage	Weight Percentage
C	66.17	58.27
O	32.62	38.27
K	1.21	3.46

Table 5.1: Data of Atomic Percentage and Weight Percentage of the pristine sample, obtained with the EDS detector of the Phenom SEM.

Then, as mentioned before, an EDS spectrum of the pristine sample A was taken to have a first approach to the characterization of the material. This corresponds to the Figure 5.4 in which, in the image a, the point on which the EDS spectrum was taken can be appreciated. In figure Figure 5.4., image b shows three elements corresponding to Carbon, Oxygen, and Potassium. Comparing it to the Table 5.4, carbon and oxygen are the most predominant elements with significant atomic and weight percentages, with a total presence of 98.79% between them. However, K has almost inconsiderable percentages, with a presence of 1.21%, so it might correspond either to a coconut shell composition or a contaminating agent; it will be proven with further characterization analysis. According to the literature, some biomaterials, such as shells and husks of different fruits, may contain minerals in their composition, such as potassium. [18] Moreover, in the image c of Figure 5.4., it can be appreciated the size distribution of the starch granules, obtained from the SEM image with specific software, showing the higher peaks between 3 μm and 4 μm , being consistent with the literature. [60]

Besides, taking a look at the Table 5.1, there is a considerable presence of carbon and oxygen, as it is reported that organic molecules such as lignin, cellulose, and starch are composed of mainly carbon and oxygen, with a bigger presence of carbon than oxygen. Converging the information between the scanning electron microscope and the electron dispersive spectrometer, it can be said that due to the presence of granules and fibers and the presence of carbon and oxygen, the composition can be assigned to be lignin, cellulose, and starch, which is consistent with the literature. [60, 18]

On the other hand, in the Figure 5.5., Figure 5.6., and Figure 5.7., the SEM images taken in the Characterization Laboratory at Yachay Tech are presented. Corresponding Figure 5.5. to be the images of the pristine sample, sample A, Figure 5.6. images of the SEM taken of sample A1T synthesized, and Figure 5.7. images of the SEM taken of

sample *A1T75* synthesized. These measurements were made to be able to compare the information obtained in the different characterization techniques of the same sample and to demonstrate that the information obtained within the two different SEM equipment is consistent at the beginning of the research and in its final stage.

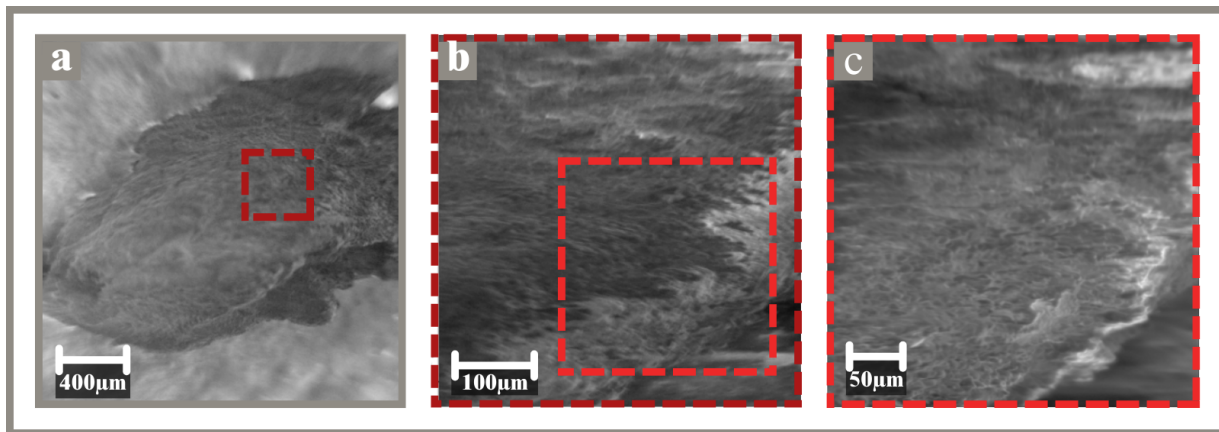


Figure 5.5: Images of sample A with the Scanning Electron Microscope integrated into an X-ray Photoelectron Spectrometer at the Characterization Laboratory at Yachay Tech. a. Image taken with an accelerating voltage of 1 kV. b. Image taken with an accelerating voltage of 3kV. c. Image taken with an accelerating voltage of 10kV.

Talking about Figure 5.5, a great visualization of the surface of the pristine material is presented; in the case of the image, a, a complete piece with a width of $1600 \mu m$ and a height of $1000 \mu m$ approximately can be observed. Then, zooming the zone to obtain image b, the granules that could be observed with the Phenon SEM on Figure 5.3 can be appreciated. More in detail, in image c, there are observed the granules and the fibers that correspond to the structural composition of the dwarf coconut as described above. Compared to the literature reported, the structure obtained in this research is confirmed to correspond to how the lignin, cellulose, and starch look in SEM images. [62]

The Figure 5.6 corresponds to the SEM images of the sample *A1T*, which can be appreciated as the synthesized zone of the sample. As the sample was prepared in the XPS sample holder, in this case, the sample was collected, crapping the pill surface, resulting in a pill breaking. Fortunately, the synthesized zone could be successfully determined. Thus, in the image a, a porous-like zone can be observed, corresponding to the synthesized zone. Then, image b is the zooming image taken, which can be better appreciated in this porous-like zone. Finally, in the image c, the structure of the material at a micro-scale can

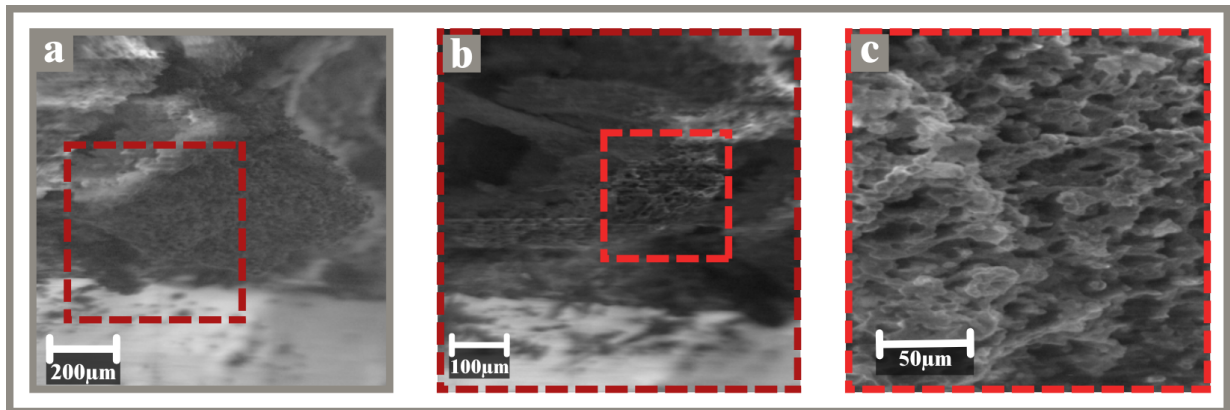


Figure 5.6: Images sample A1T with the Scanning Electron Microscope integrated into an X-ray Photoelectron Spectrometer at the Characterization Laboratory at Yachay Tech. a. Image taken with an accelerating voltage of 1kV. b. Image taken with an accelerating voltage of 1kV. c. Image taken with an accelerating voltage of 10kV.

be completely appreciated. It can be confirmed that the structure presents well-distributed porosity and granules are present. Those granules may have come from the starch composition of the material, which, during the synthesis process, would have served as a base precursor for forming the hard carbon material. [63]

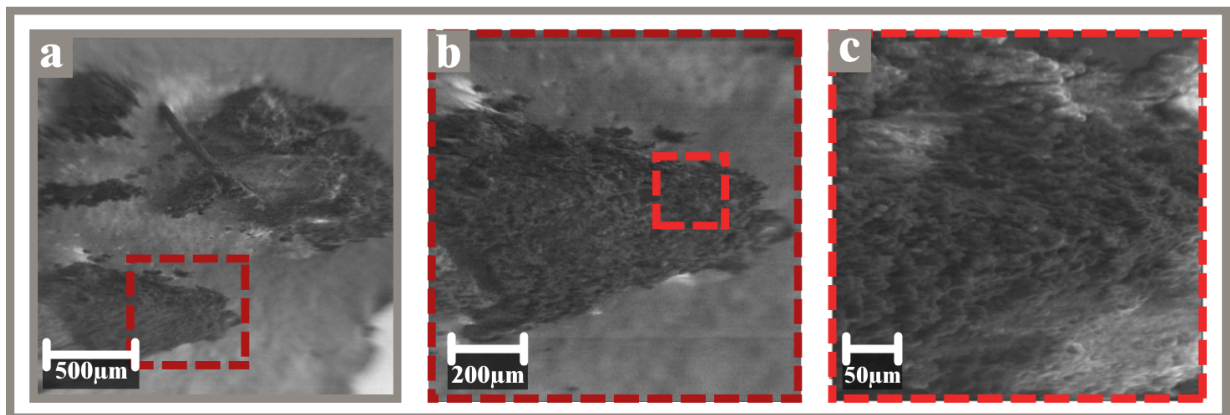


Figure 5.7: Images sample A1T75 with the Scanning Electron Microscope integrated into an X-ray Photoelectron Spectrometer at the Characterization Laboratory at Yachay Tech. a. Image taken with an accelerating voltage of 1kV. b. Image taken with an accelerating voltage of 1kV. c. Image taken with an accelerating voltage of 1kV. d. Image taken with an accelerating voltage of 10kV.

Following the path, the Figure 5.7 corresponds to the synthesized sample *A1T75*, which corresponds to a smaller particle size than the sample analyzed above, sample *A1T*. Then, in the image a of Figure 5.7, the sample can be appreciated in general, there can be distinguished its porous-like structure in the different zones observed in the image. Moreover, in

image b, zooming was made to observe the structure of this sample better. In image c, the structure can be appreciated more in detail due to the zoomed-up. As well as on image c of Figure 5.6, the well-distributed porous can be observed. According to the literature, it is said that hard carbon nanostructures, at a microscale, appear to be porous-like materials, which can be compared to the information obtained with the SEM images. [64]

5.3 Raman Spectroscopy

The Raman spectra of the samples were taken mostly with the green laser, corresponding to the 532 nm wavelength laser; however, to measure the pristine sample, the 785 nm wavelength laser was also used. In the Figure 5.8, three different Raman spectra correspond to the measurements made to the three samples. The image *a* corresponds to the spectra of sample *A*, the pristine sample with the two lasers, 532 nm and 785 nm wavelength. The two different lasers were used because the 532nm laser would follow the research path to examine samples with the same conditions and parameters, but it did not work. Then, as sample *A* corresponds to the pristine sample, the coconut shell, the 785 nm laser was used because it is a biomass containing organic molecules, and, according to the literature, it is recommended. Even though two different wavelengths were used to measure the pristine sample, no information was obtained about this sample with this characterization technique.

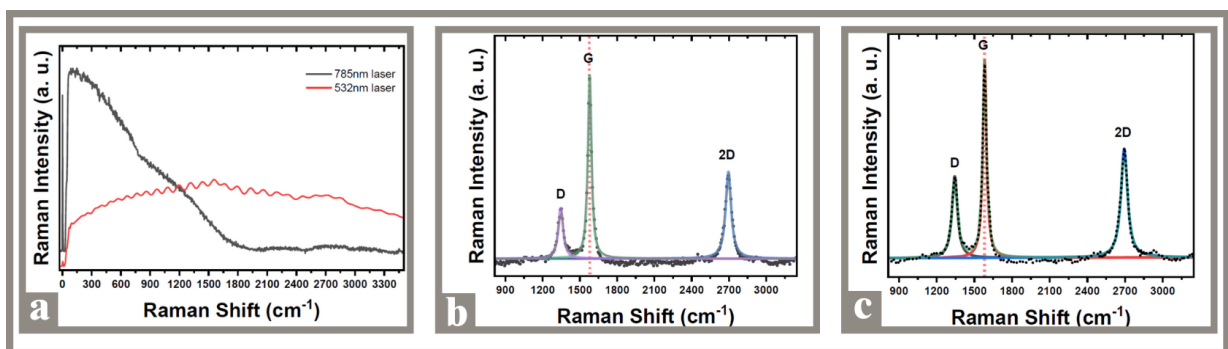


Figure 5.8: Raman spectra of a. Pristine sample *A* measured with laser 532 nm and 785nm. b. Spectrum of the synthesized sample *A1T*, measured with laser 532 nm, and its corresponding deconvolution. c. Spectrum of the synthesized sample *A1T*, measured with laser 532 nm, and its corresponding deconvolution.

On the other hand, the images *b* and *c* of the Figure 5.8 correspond to the samples

A1T and *A1T75* synthesized, respectively, and those spectra were taken with the laser of 532 nm wavelength. According to the literature, carbon-based materials, especially graphite-like structures, should present on their Raman spectra at least three different peaks, called bands. Those bands correspond to the *D band* with its center located around 1350 cm^{-1} , *G band* located around 1580 cm^{-1} , and the *2D band* located at 1690 cm^{-1} . Summarizing the meaning of the bands, the *D band* indicates the proportion of defects and amorphous material present in the carbon-like structure; the *G band* is the one which indicates the presence of a carbon-based material; and the *2D band* indicates if there are present graphene structures in the carbon-based material, to asses to a specific material, it will depend on the intensity of the peaks.

Moreover, it has to be understood when a Raman spectrum corresponds to a hard carbon nanostructure. The first thing to notice is the presence of the three bands mentioned above, the *D band*, the *G band*, and the *2D band*. Then, to see if the intensities of the peaks are correct, they can be estimated with the I_D/I_G ratio, which, depending on the value, may correspond to an organized structure, a crystal structure, or an amorphous structure. This ratio ensures the amorphycity rate present in samples. The value that this ratio usually takes is in a range of 0.5 to 0.9 in the case of hard carbon nanostructures.

Sample	Peak Center (cm^{-1})	Band Assignment	FWHM (cm^{-1})
A1T	1345.93	D	46.17
A1T	1578.97	G	34.57
A1T	2695.61	2D	53.74
A1T75	1343.85	D	52.06
A1T75	1582.32	G	35.29
A1T75	2693.28	2D	62.68

Table 5.2: Data of the peaks obtained of Raman analysis.

As shown on images *b* and *c* of Figure 5.8, the three bands mentioned above are present: the *D band*, *G band*, and *2D band*. The center of each peak shown is on the Table 5.2. This information is important to assess which material is present in the Raman characterization.

Moreover, looking at figure *b* of Figure 5.8, three clear peaks can be appreciated, corresponding to the *D band*, *G band*, and *2D band*. In this image, the dashed line guided to the eye is placed 1578.97 cm^{-1} corresponding to the center of the *G band*, the value obtained after the Raman spectra deconvolution of sample *A1T*. Then, in the image *c*, the

dashed line guided to the eye is placed at 1582.32 cm^{-1} that corresponds to the center of the *G band* of a sample *A1T75*. Then, according to the literature, the *G band* should be located at 1580 cm^{-1} , however, as Raman may present an error of $\pm 1 \text{ cm}^{-1}$, that results on the correct *G band* assignments for sample *A1T*, and for *A1T75*. [65].

About the *2D band* of the two different samples, *A1T* of image *b*, and *A1T75* of image *c*, their center is located at 2695.61 cm^{-1} , and 2695.61 cm^{-1} respectively. It has been reported that information about the amount of graphene layers can be extracted depending on the full width at half maximum (FWHM) of these peaks. In the case of sample *A1T*, the *2D* peak is located at 2695.61 cm^{-1} , and its FWHM corresponds to 53.74 cm^{-1} . For sample *A1T75*, the *2D* peak is located at 2693.28 cm^{-1} , and its FWHM corresponds to 62.68 cm^{-1} . Interpreting the values presented, sample *A1T* will tend to have fewer graphene layers than sample *A1T75* because of the FWHM value. However, the FWHM present on the different spectra is too big to be suitable for analyzing the number of graphene layers in the structure. [66]

In the Raman spectra of the samples *A1T* and *A1T75*, see Figure 5.8, the *D band* are predominant peaks. The *D band* corresponds to the material 'defects,' which can be assessed to sp^2 hybridization of the carbon atom. In the case of sample *A1T*, the *D band* is located at 1345.93 cm^{-1} , and for the sample *A1T75*, the *D band* is located at 1343.85 cm^{-1} . It has been reported that the position of the *D band* in hard carbon nanostructures may vary depending on the structure of the material, but it might be found around 1350 cm^{-1} . Then, with the *D band*, the information about the level of graphitization of a carbonous structure can be determined, giving information about the presence of more amorphous carbon as predominant as this peak is. [63]

Finally, the I_D/I_G ratio of the spectra will provide information about the degree or disorder within the hard carbon nanostructures. For sample *A1T*, the I_D/I_G ratio is equal to 0.25, and the I_D/I_G ratio for sample *A1T75* is 0.41. Thus representing for *A1T* a lower level of disorder in its structure than sample *A1T75*. [67] Finally, with this Raman spectroscopy analysis and converging the information with the obtained from scanning electron microscopy, the characteristics obtained for samples *A1T* and *A1T75* can be assessed to hard carbon nanostructures, but it is needed to extract more information from other characterization techniques to prove this statement. [68]

5.4 X-Ray Photoelectron Spectroscopy

In this section, the X-ray Photoelectron Spectroscopy analysis is presented. To begin with, in Figure 5.9, the XPS spectra of samples *A*, *A1T*, and *A1T75* are presented. Figure a, b, and c correspond to the survey spectra of the samples mentioned. In this type of spectra, the information that can be obtained corresponds to the information of the elements in the sample. Noticeably, three main elements are present: C1s, O1s, and N1s. The atomic concentration of each sample is presented in the Table 5.3.

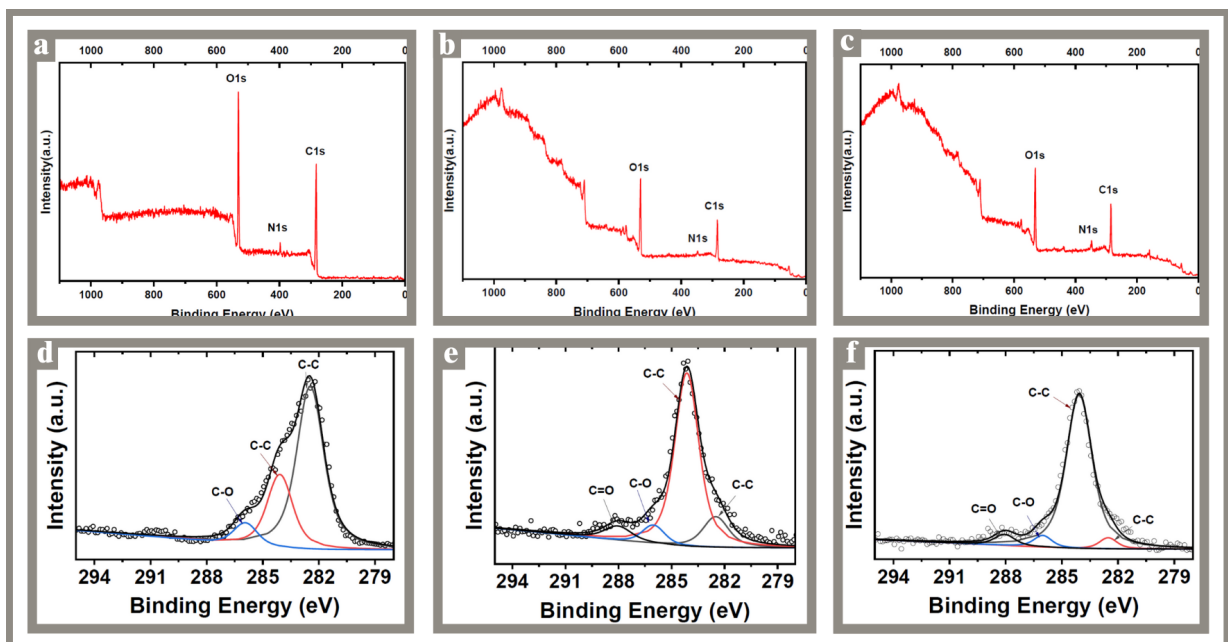


Figure 5.9: XPS survey spectra and C1s analysis of each sample a. Survey of pristine sample *A*. b. Survey of the synthesized sample *A1T*. Survey of synthesized sample *A1T75*. d. C1s spectra of sample *A*. e. C1s spectra of sample *A1T*. f. C1s spectra of sample *A1T75*.

Looking at the Table 5.3, the most predominant element in all samples is carbon. However, it corresponds to different structures. Sample *A* has 75.5 % of carbon, 23.3 % of oxygen, and 3.2 % of nitrogen. These results are not equal to the EDS results obtained (see Table 5.1), but the information is consistent with the literature. Biomaterials, such as coconut husk from *Cocos Nucifera* species, are reported to have around 65 to 75% of carbon on their structure and around 20 to 25 % of oxygen on their structure, and the remaining percentage might correspond to functional groups containing nitrogen or to mineral impurities. [69] Those percentages in these materials mentioned are reported to

correspond to cellulose, lignin, and starch.

Sample	C %	O %	N %
A	73.5	23.3	3.2
A1T	87.8	11.8	0.4
A1T75	78.2	20.2	1.6

Table 5.3: Atomic concentration table of samples *A*, *A1T*, and *A1T75*, obtained from XPS measurements.

Moreover, looking at samples *A1T* and *A1T75* of Table 5.3, there is a change in the atomic percentage of all the elements. For sample *A1T*, carbon is increased to 87.8%, a difference of 14.3 % on the atomic percentage increase of carbon, the percentage of oxygen decreased on 11.5 %, reaching the 11.8 % of oxygen in the sample; and, nitrogen percentage decreased to reach the 0.4 % which means that was almost eliminated during the synthesis process. On the other hand, the percentages for sample *A1T75* changed differently. For the atomic percentage of carbon, the value increased to be 78.2 %, increasing just in 4.7 %; oxygen decreased to reach 20.2; and nitrogen decreased exactly half the amount from the pristine sample, reaching 1.6 % of nitrogen. This information corresponds to reported percentages of hard carbon nanostructures obtained from natural sources. However, it has to be consistent with the high-resolution spectra to see which changes in the bonds present in the material.

Sample	Peak Energy (eV)	Peak Assignment
A	282.46	C-C [70]
A	284.08	C-C [71]
A	285.92	C-O [72]
A1T	282.49	C-C [70]
A1T	284.13	C-C [71]
A1T	286.03	C-O [72]
A1T	288.04	C=O [73]
A1T75	282.53	C-C [70]
A1T75	284.07	C-C [71]
A1T75	286.02	C-O [72]
A1T75	288.06	C=O [73]

Table 5.4: Peak assignment table of the C1s high-resolution spectra obtained from XPS.

Assigning the peaks to each different sample, it can be observed in Table 5.4 that three

peaks are assigned for the sample *A*. The 282.46 eV corresponds to a $C - C$ bond corresponding to an amorphous-like structure, with sp^2 hybridization. [70] Then, the 284.08 eV peak corresponds to a sp^2 well arranged $C - C$ bond. According to the literature, this peak assignment may correspond to the bonds present in organic molecules and converged with the information mentioned in Table 5.3, and this might be assigned to the bonds contained in lignin, cellulose, and starch molecules.

Talking about sample *A1T*, looking at Table 5.4, the peak location and assignment correspond to be 282.49 eV for the $C - C$ bond, which corresponds to an amorphous-like structure [74]; the 284.13 eV peak is assigned to be the $C - C$ bond of a sp^2 hybridization, characteristic of well-arranged structures of carbon. And the 282.53 eV peak corresponds to a $C = O$ bond. [75, 64, 66, 73]

As in sample *A1T*, almost an equal case was obtained for sample *A1T75*. For the 282.49 eV peak corresponds to the $C - C$ bond in an amorphous-like structure[74]; the 284.07 eV peak is assigned to be a $C - C$ bond of a sp^2 hybridization; then, the 286.02 eV peak is the $C - C$ bond corresponding; finally, the 288.06 eV in the peaks which correspond to the $C = O$ [75, 64] bonding. [66].

Having clear information about the location of the peaks in each sample, the spectra of the samples can be compared. In the pristine sample, the most predominant peak corresponds to the $C - C$ peak of amorphous carbon, and the peak corresponds to the $C - C$ bond characteristic of well-arranged carbon atoms in the structure. Thus, giving information of a low well-arrangement of the atoms in the structure of the pristine sample. Then, following this path, in the case of the sample *A1T* and *A1T75*, a complete change in the spectra can be appreciated, compared with sample *A.A* [76]. In these samples, *A1T* and *A1T75*, the most predominant peak comes to be the $C - C$ peak of a well-arranged structure, saying then that the synthesis was correct.

5.5 X-Ray Diffraction

Three different spectra were obtained in this characterization technique as observed in Figure 5.10. This figure presents the corresponding diffractograms of the three different samples, *A*, *A1T*, and *A1T75*. As XRD is a characterization technique that analyzes

mostly the crystallinity of the materials, looking at the diffractogram *A* of Figure 5.10 that correspond to the pristine sample, it can not be appreciated or distinguished predominant peaks because there are many organic molecules arranged in a disorganized way causing the non-definition of the diffractogram. However, a peak with $\theta^\circ = 22^\circ$ center can be observed. It has been reported that this plane (002) may correspond to carbon-based organic materials such as aligning, cellulose, and starch. [18]

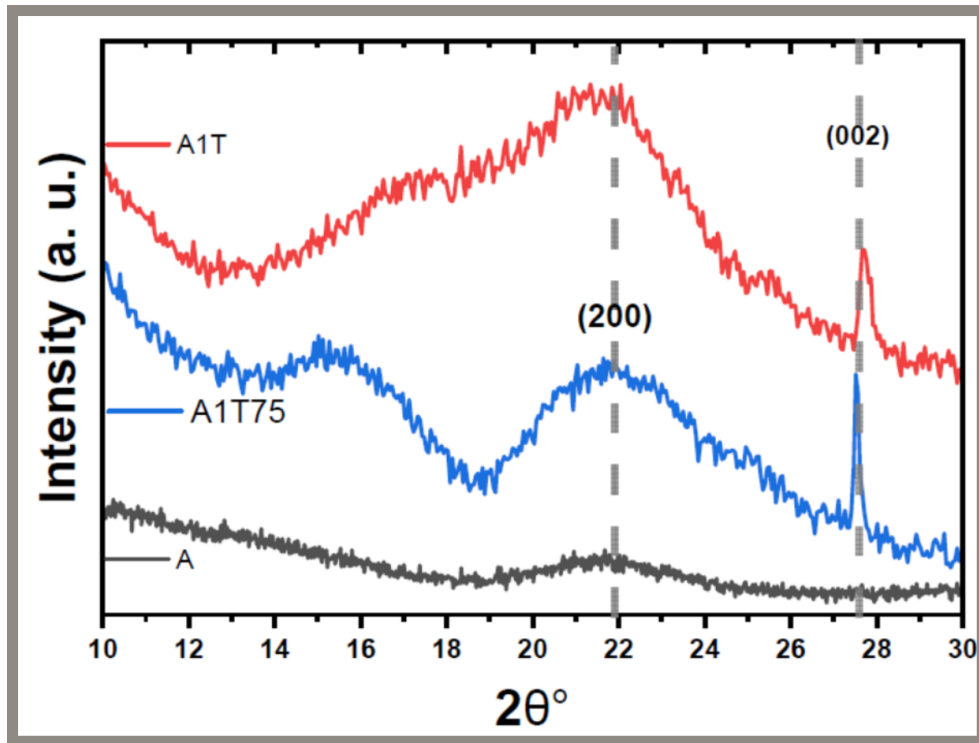


Figure 5.10: XRD diffractogram of samples *A*, *A1T*, and *A1T75*.

There are some differences between the samples; the most predominant is that in the pristine sample, *A*, there can not be distinguished predominant curves or peaks; however, after the synthesis process, the diffractograms change completely. Looking at the diffractograms of samples *A1T* and *A1T75*, samples corresponding after the synthesis process, there arise some peaks corresponding to the (200) and (002) as seen in the Figure 5.10. According to reported literature, at the interval of $2\theta^\circ = 22^\circ$ to 24° , the (200) plane is located, which corresponds mostly to a carbon-based material highly disordered structure or amorphous carbon. This peak is also reported to belong to cellulose and starch structures. [12] Then, the center of the peaks are $2\theta = 21.7^\circ$ for sample *A1T* $2\theta = 21.8^\circ$ for sample *A1T75*. [77, 78] And the dashed line guided to the eye is placed at 22° to have an

orientation for locating the (200) plane. The second dashed line guided to the eye is placed to have an orientation to the (002) plane location at $2\theta = 27.5^\circ$. This peak indicates the level of graphitization of the structure, meaning the presence of graphene layers. [62]

Based on the (002) plane peak center and using Bragg's Law, the interplanar distances of the planes present in the sample structure can be estimated. The expected interplanar distances in hard carbon nanostructures may vary. It has been reported to have distances from 0.36 nm to 0.44 nm. [63, 79] In this research, for sample *A1T*, the (002) peak center obtained was $2\theta = 27.8^\circ$, and for sample *A1T75* the (002) peak center obtained was $2\theta = 27.7^\circ$. Besides, Bragg's Law states the relation between the spacing of atomic planes in crystalline structures and the angles of incidence, followed by the equation $n\lambda = 2d\sin(\theta)$. Where n is the order of the diffraction peak (usually takes a value of 1 for the first-order diffraction), λ is the wavelength of the incident X-rays, d is the interplanar distance, and θ is the angle between the incident X-ray beam and the crystal planes (half of the measured 2θ angle). To calculate the interplanar distance, the wavelength corresponding to the XRD source, *Cu K α* , used in the research is $\lambda = 1.54 \text{ \AA}$. Then, the interplanar distances obtained for each sample are, for the sample *A1T*, $d_{A1T} = 4.1 \text{ \AA}$, and for the sample *A1T75*, $d_{A1T75} = 4.0 \text{ \AA}$.

5.6 Transmission Electron Microscopy

All the information extracted from the different characterization techniques in this section converges. Transmission Electron Microscopy (TEM) is an analytical characterization technique in which the structures of materials can be visualized. Multiple TEM images of samples *A1T* and *A1T75* were obtained; however, when it was intended to take a TEM image of sample *A* pristine, the material ended up due to the high accelerating voltage used.

Analyzing Figure 5.11, the image *a* presents the structure of hard carbon nanostructures; it can be differentiated from the grating used because in the upper part of the image is distinguished the amorphous carbon coming from the grating. Then, looking at the image from the middle to the bottom, there are hard carbon nanostructures. To have a better understanding image *b* is a zooming from the center zone of the image *a*, there can be ap-

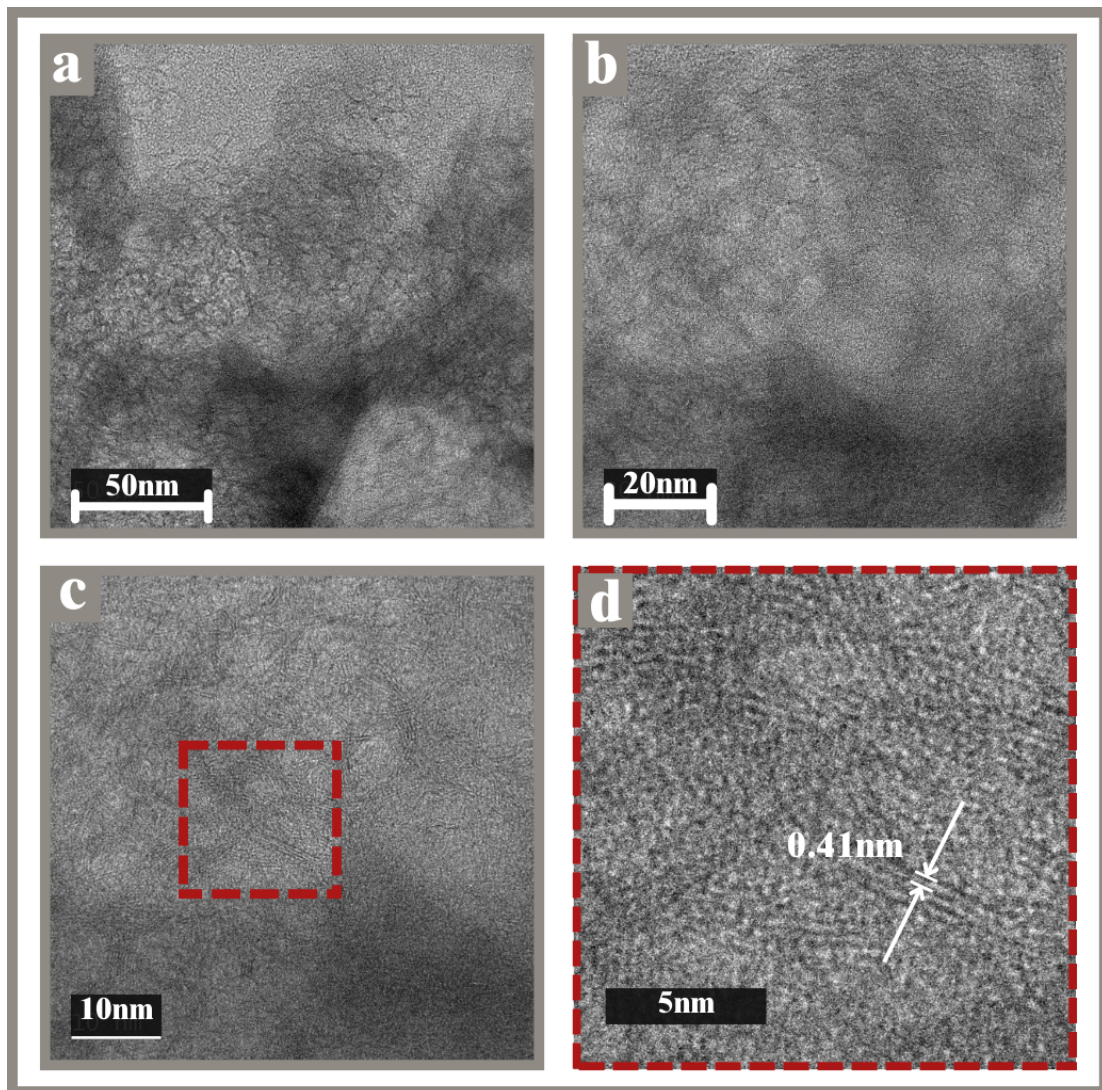


Figure 5.11: TEM images of sample *A1T*. a., b., and c., images are presented in zooming order; those were taken directly with the TEM to understand the material better. d. Image zoomed from c, interplanar distance present.

preciated circumferential zones that, comparing to the information obtained from SEM, it may correspond to the porosity of the material. This mentioned can be better appreciated in image c. Then, image d is a zooming image from c, there can be noticed well-arranged structures, comparing with the literature reported this corresponds to the hard carbon nanostructures. [79, 80] Then, describing the structures, there can be noticed well-defined planes that corresponds to graphene layers, these layers are packed with a number from at least 4 to 8 layers, as observed. Comparing this information with Raman spectra, it is supposed that when having few graphene layers, it can be estimated the exact number with the *2D band*; however, this can not be done in for this structure because of the too big

with of the peak and of the noncomplete crystallinity of the hard carbon nanostructures. Thus, the TEM technique is suitable for developing this estimation. [78, 81]

To analyze and measure the interplanar distances, it was taken fifty distances found in the image *d* of Figure 5.11, obtaining a final average of 0.41 nm or 4.1 \AA that, according to the literature is on range of interplanar distances in hard carbon nanostructures reported. This information also converges completely with the information obtained from the XRD technique. [63, 79]

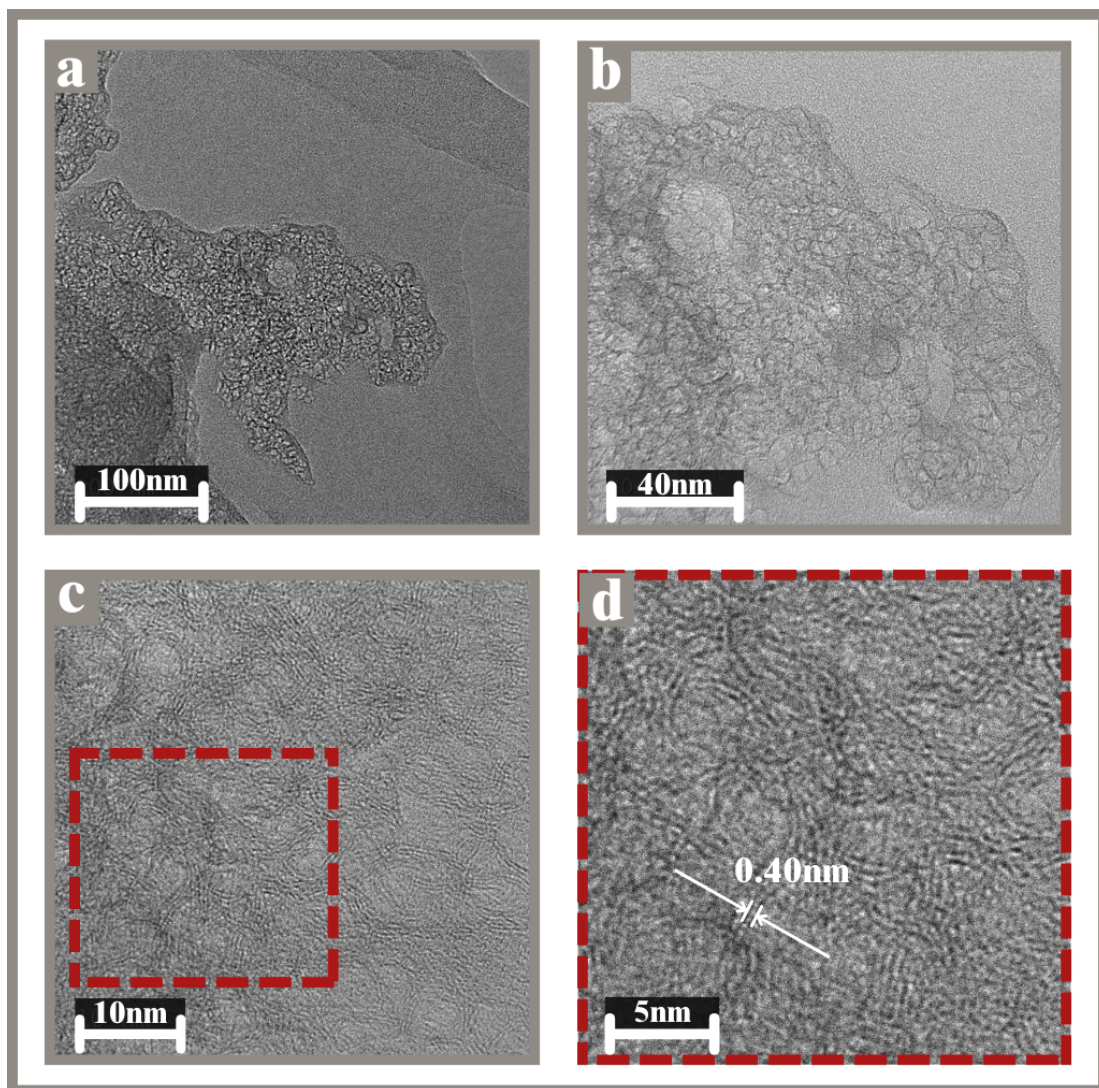


Figure 5.12: TEM images of sample *A1T75*. a., b., and c., images are presented in zooming order, those were taken directly with the TEM, to understand the material better. d. Image zoomed from c, interplanar distance present.

Besides, analyzing image Figure 5.12, in the image a, it can be better distinguish the hard carbon nanostructures, which are centered in the image. Approaching the hard carbon

nanostructures zone appears in image b, where a better visualization of the structure is observed. Then, in image c, similarly to image c of Figure 5.11, there can be noticed the circumferential zones that, compared to the information obtained from SEM, this structure could correspond to the porosity of the material. This mentioned can be better appreciated in image c. Then, image d is a zooming image from c, and well-arranged structures can be observed, which corresponds to the hard carbon nanostructures reported in the literature. [79]

Then, describing the hard carbon structures, looking at image d of Figure 5.12, one can notice well-defined planes that correspond to graphene layers; as in sample *A1T*, these layers are packed with a number from at least 4 to 12 layers, as observed. When comparing this information with Raman spectra, it is supposed that when there are only a few graphene layers, the exact number can be estimated using the *2D band*. However, this cannot be done in this structure because of the excessive peak width and the semi-crystallinity of the hard carbon nanostructures. Therefore, the TEM technique is more suitable for making this estimation. [78, 81] Thus, the interplanar distance of the sample *A1T75* hard carbon nanostructures was estimated, as for sample *A1T*, where there were taken fifty different interplanar distances from the image d of Figure 5.12, and an average of 0.40 nm or 4.0 \AA was obtained. According to the literature this measured value is in the range of interplanar distances in hard carbon nanostructures reported. This information also converges completely with the information obtained from the XRD technique for sample *A1T75*. [63, 79]

Chapter 6

Conclusions

To conclude this research, the objectives stated were accomplished. First, a green synthesis methodology was successfully developed to obtain hard carbon nanostructures by laser ablation. This included the implementation of using bio-waste material, the *Parajubaea Cocoides* fruit (specifically its shell or husk), as a precursor for the carbon-based nanostructures obtained. The methodology consisted of using physical methods to have the sample suitable for the synthesis process, and the technique used to synthesize the material was laser ablation, obtaining the hard carbon nanostructures. The parameters for the synthesis were established successfully in the research.

Then, five different characterization techniques were employed to ensure the material was hard carbon nanostructures: SEM, Raman Spectroscopy, XPS, XRD, and TEM. Starting from the pristine material, which corresponded to the *Parajubaea Cocoides* coconut husk, the SEM technique found the presence of amorphous and similar-sized granules and fibers. This contrasted with the literature, with the XRD results, and with the XPS results; the granules were assigned to have a starch and cellulose composition, and the fibers were composed of lignin and cellulose. With the composition mentioned, this coconut shell or husk is suitable for being a precursor material to synthesize hard carbon nanostructures due to the molecules having a high carbon content in their structure. The results enclosing *Parajubaea Cocoides* fruit waste or bagasse can be implemented as a potential hard carbon nanostructure precursor due to its very high compound content, which contains a high carbon percentage in its components. However, it must be mentioned that due to the composition of various organic molecules in the coconut shell structure, information

could not be obtained from Raman spectroscopy and transmission electron microscopy characterization techniques.

On the contrary, talking about the synthesized samples, the information from the five different characterization techniques was obtained and converged between them. First, SEM images showed a porous-like structure, which could be observed in those porous distributed homogeneously. Compared to the literature, the material shown in the SEM images coincides with the reported hard carbon images. And, looking at how the material changed, the structure changed from being a granules-like structure in the pristine sample *A* to a porous-like structure in samples *A1T* and *A1T75*. About Raman Spectroscopy, it has to be noticed that the Raman spectra from hard carbon showed the presence of carbonous materials by revealing a clean spectrum with the *D band*, *G band*, and *2D band*, being sharp and thin peaks similar to graphite/graphene spectra. In the case of the *D band* and *G band*, the peaks showed an excellent intensity with different sizes, with the *D band* much shorter than the *G band* band, with an I_D/I_G ratio of 0.25, in the case of sample *A1T*. An I_D/I_G ratio of 0.41 in the case of sample *A1T75* was obtained. This information showed that the structures have graphite and amorphous carbon on them. However, in the case of the *2D band*, even though the intensity was lower than the *G band* but bigger than the *D band* and relatively sharp, with an $FWHM = 53.74 \text{ cm}^{-1}$ for the sample *A1T*, and a $FWHM = 62.68 \text{ cm}^{-1}$ for sample *A1T75*, revealing the presence of very few-layer graphene on both cases, but there could not be estimated the amount of the layers due to it was not sharp enough to be compared with the literature reported. Moreover, the *XPS*, the analysis of the pristine sample, showed the presence of primarily carbon and oxygen, with amorphous $C-C \text{ sp}^2$ bonds in the majority, and $C-C \text{ sp}^2$ bonds corresponding to graphitic/arranged structure in a lower amount, matching the organic composition of the *Parajubaea Cocoides* (starch, lignin and cellulose). As desired, the laser-annealed hard carbon showed a more robust $C-C \text{ sp}^2$ graphitic carbon structure. Besides, according to the *XRD* analysis, some planes (002) correspond to graphitic structures with well-arranged planes but with different inter-planar distances; the estimated interplanar distances calculated with Bragg's law was 0.41 nm for sample *A1T* and 0.40 nm for sample *A1T75*. The *TEM* analysis confirmed the information obtained with *XRD* and the predicted structure hard carbon nanostructures would present. The images support the *XRD* results by showing that the material contains

aligned graphitic planes, with few layers of graphene, with a mean inter-planar distance of 0.41 *nm* for sample *A1T* and 0.40 *nm* for sample *A1T75*. Then, it can be concluded that the structure of hard carbon nanostructures corresponds to material containing amorphous carbon, graphite, and graphene, forming enclosed zones, a few graphene with short lengths arranged as small walls, randomly distributed and filled with amorphous carbon. This structure lets the structure have vacancies.

Finally, the characterization analysis conducted on the hard carbon nanostructures demonstrates that *Parajubaea Cocoides* has starch, lignin, and cellulose in its structure, being a suitable precursor to synthesize hard carbon nanostructures. Then, the laser ablation synthesis method was shown to be accurate when synthesizing hard carbon nanostructures. Moreover, hard carbon nanostructures are shown to be a semi-crystal nanostructure that presents amorphous carbon and vacancies enclosed between enlarged surface areas formed by graphene layers. Finally, as it was proved that these nanostructures correspond to hard carbon, they may serve as an ion-storage material as a potential replacement for anodes in solid-state batteries. Future work using hard carbon nanostructures would be involving building a hard carbon anode in the laboratory to demonstrate its functionality as a potential replacement for the mentioned solid-state batteries.

Bibliography

- [1] A. Beda, J.-M. Le Meins, P.-L. Taberna, P. Simon, and C. M. Ghimbeu, “Impact of biomass inorganic impurities on hard carbon properties and performance in na-ion batteries,” *Sustainable Materials and Technologies*, vol. 26, p. e00227, 2020.
- [2] L. Xie, C. Tang, Z. Bi, M. Song, Y. Fan, C. Yan, X. Li, F. Su, Q. Zhang, and C. Chen, “Hard carbon anodes for next-generation li-ion batteries: review and perspective,” *Advanced Energy Materials*, vol. 11, no. 38, p. 2101650, 2021.
- [3] A. Baldinelli, X. Dou, D. Buchholz, M. Marinaro, S. Passerini, and L. Barelli, “Addressing the energy sustainability of biowaste-derived hard carbon materials for battery electrodes,” *Green chemistry*, vol. 20, no. 7, pp. 1527–1537, 2018.
- [4] C. D. Liyanage and M. Pieris, “A physico-chemical analysis of coconut shell powder,” *Procedia Chemistry*, vol. 16, pp. 222–228, 2015.
- [5] S. Park, J. Song, W. C. Lee, S. H. Jang, J. Lee, J. Kim, H.-K. Kim, and K. Min, “Advances in biomass-derived electrode materials for energy storage and circular carbon economy,” *Chemical Engineering Journal*, p. 144234, 2023.
- [6] P. Karthik, A. Himaja, and S. P. Singh, “Carbon-allotropes: synthesis methods, applications and future perspectives,” *Carbon letters*, vol. 15, no. 4, pp. 219–237, 2014.
- [7] A. Hirsch, “The era of carbon allotropes,” *Nature materials*, vol. 9, no. 11, pp. 868–871, 2010.
- [8] M. Dalal, *A Textbook of Inorganic Chemistry–Volume 1*. Dalal Institute, 2017.
- [9] R. Mallion and D. Rouvray, “Molecular topology and the aufbau principle,” *Molecular Physics*, vol. 36, no. 1, pp. 125–128, 1978.

- [10] A. Barabash, “Experimental test of the pauli exclusion principle,” *Foundations of Physics*, vol. 40, no. 7, pp. 703–718, 2010.
- [11] D. Xue, C. Sun, and X. Chen, “Hybridization: a chemical bonding nature of atoms,” *Chinese Journal of Chemistry*, vol. 35, no. 9, pp. 1452–1458, 2017.
- [12] W. Lv, F. Wen, J. Xiang, J. Zhao, L. Li, L. Wang, Z. Liu, and Y. Tian, “Peanut shell derived hard carbon as ultralong cycling anodes for lithium and sodium batteries,” *Electrochimica Acta*, vol. 176, pp. 533–541, 2015.
- [13] Z. Liu, T. Lu, and Q. Chen, “An sp-hybridized all-carboatomic ring, cyclo [18] carbon: Bonding character, electron delocalization, and aromaticity,” *Carbon*, vol. 165, pp. 468–475, 2020.
- [14] Z. Zhang, J. Zhang, G. Kwong, J. Li, Z. Fan, X. Deng, and G. Tang, “All-carbon sp-sp² hybrid structures: Geometrical properties, current rectification and current amplification,” *Scientific Reports*, vol. 3, no. 1, p. 2575, 2013.
- [15] N. Hernández, R. C. Williams, and E. W. Cochran, “The battle for the “green” polymer. different approaches for biopolymer synthesis: bioadvantaged vs. bioreplacement,” *Organic & biomolecular chemistry*, vol. 12, no. 18, pp. 2834–2849, 2014.
- [16] J. T. McNamara, J. L. Morgan, and J. Zimmer, “A molecular description of cellulose biosynthesis,” *Annual review of biochemistry*, vol. 84, pp. 895–921, 2015.
- [17] D. Das, S. Hussain, A. K. Ghosh, and A. K. Pal, “Studies on cellulose nanocrystals extracted from musa sapientum: Structural and bonding aspects,” *Cellul Chem Technol*, vol. 52, no. 9–10, pp. 729–739, 2018.
- [18] C. U. Maheswari, K. O. Reddy, E. Muzenda, B. Guduri, and A. V. Rajulu, “Extraction and characterization of cellulose microfibrils from agricultural residue–cocos nucifera l.” *Biomass and bioenergy*, vol. 46, pp. 555–563, 2012.
- [19] A. Tolbert, H. Akinosho, R. Khunsupat, A. K. Naskar, and A. J. Ragauskas, “Characterization and analysis of the molecular weight of lignin for biorefining studies,” *Biofuels, Bioproducts and Biorefining*, vol. 8, no. 6, pp. 836–856, 2014.

- [20] Q. Peng, K. Wang, Y. Gong, X. Zhang, Y. Xu, Y. Ma, X. Zhang, X. Sun, and Y. Ma, "Tailoring lignin-derived porous carbon toward high-energy lithium-ion capacitor through varying sp²-and sp³-hybridized bonding," *Advanced Functional Materials*, vol. 33, no. 52, p. 2308284, 2023.
- [21] S. Pérez and E. Bertoft, "The molecular structures of starch components and their contribution to the architecture of starch granules: A comprehensive review," *Starch-Stärke*, vol. 62, no. 8, pp. 389–420, 2010.
- [22] M. Zhao, B. Li, J.-X. Cai, C. Liu, K. McAdam, and K. Zhang, "Thermal & chemical analyses of hydrothermally derived carbon materials from corn starch," *Fuel Processing Technology*, vol. 153, pp. 43–49, 2016.
- [23] C. Lee, X. Wei, J. W. Kysar, and J. Hone, "Measurement of the elastic properties and intrinsic strength of monolayer graphene," *science*, vol. 321, no. 5887, pp. 385–388, 2008.
- [24] A. R. Oganov, R. J. Hemley, R. M. Hazen, and A. P. Jones, "Structure, bonding, and mineralogy of carbon at extreme conditions," *Reviews in Mineralogy and Geochemistry*, vol. 75, no. 1, pp. 47–77, 2013.
- [25] D. Sederberg, L. Bryan, and N. Giordano, "Allotropes of carbon," *It's all in the way you're put together. Retrieved [insert date] from [http://www. physics. purdue. edu/psas](http://www.physics.purdue.edu/psas)*, 2009.
- [26] K. Hembram, S. Lee, H. Im, H. Ju, S.-H. Jeong, and J.-K. Lee, "The surface hybridization of diamond with vertical graphene: a new route to diamond electronics," *Materials Horizons*, vol. 7, no. 2, pp. 470–476, 2020.
- [27] B. J. Garrison, E. J. Dawnkaski, and D. W. Srivastava, Deepak, "Molecular dynamics simulations of dimer opening on a diamond {001}(2x1) surface," *Science*, vol. 255, no. 5046, pp. 835–838, 1992.
- [28] B. Xiao, T. Rojo, and X. Li, "Hard carbon as sodium-ion battery anodes: progress and challenges," *ChemSusChem*, vol. 12, no. 1, pp. 133–144, 2019.

- [29] J. Li, C. Peng, J. Wang, J. Li, and H. Zhang, "Towards an atomistic understanding of hard carbon electrode materials and sodium behaviors," *Diamond and Related Materials*, vol. 129, p. 109355, 2022.
- [30] J. Zou, K. Reichelt, K. Schmidt, and B. Dischler, "The deposition and study of hard carbon films," *Journal of applied physics*, vol. 65, no. 10, pp. 3914–3918, 1989.
- [31] H. Zhang, I. Hasa, and S. Passerini, "Beyond insertion for na-ion batteries: nanostructured alloying and conversion anode materials," *Advanced Energy Materials*, vol. 8, no. 17, p. 1702582, 2018.
- [32] X. Zhu, X. Jiang, X. Liu, L. Xiao, and Y. Cao, "A green route to synthesize low-cost and high-performance hard carbon as promising sodium-ion battery anodes from sorghum stalk waste," *Green Energy & Environment*, vol. 2, no. 3, pp. 310–315, 2017.
- [33] K. Schutjajew, P. Giusto, E. Härk, and M. Oschatz, "Preparation of hard carbon/-carbon nitride nanocomposites by chemical vapor deposition to reveal the impact of open and closed porosity on sodium storage," *Carbon*, vol. 185, pp. 697–708, 2021.
- [34] M. Drews, J. Büttner, M. Bauer, J. Ahmed, R. Sahu, C. Scheu, S. Vierrath, A. Fischer, and D. Biro, "Spruce hard carbon anodes for lithium-ion batteries," *ChemElectroChem*, vol. 8, no. 24, pp. 4750–4761, 2021.
- [35] X. Dou, "Hard carbon anode materials for sodium-ion battery," Ph.D. dissertation, Karlsruher Institut für Technologie (KIT), 2019.
- [36] Y. Zhen, Y. Chen, F. Li, Z. Guo, Z. Hong, and M.-M. Titirici, "Ultrafast synthesis of hard carbon anodes for sodium-ion batteries," *Proceedings of the National Academy of Sciences*, vol. 118, no. 42, p. e2111119118, 2021.
- [37] M. Deng, W. Dong, and F. Huang, "High initial coulombic efficiency hard carbon anodes enabled by facile surface annealing engineering," *Chemistry—An Asian Journal*, p. e202300210, 2023.
- [38] I. Alexandrou, I. Zergioti, G. Amaratunga, M. Healy, C. Kiely, P. Hatto, M. Velegarakis, and C. Fotakis, "A new reactive pulsed laser ablation technique for the deposition of

- hard carbon and carbon-nitride thin films,” *Materials Letters*, vol. 39, no. 2, pp. 97–102, 1999.
- [39] A. Jo, B. Lee, B. G. Kim, H. Lim, J. T. Han, S. Y. Jeong, J. Kim, S. H. Seo, H. J. Jeong, G.-W. Lee *et al.*, “Ultrafast laser micromachining of hard carbon/fumed silica anodes for high-performance sodium-ion capacitors,” *Carbon*, vol. 201, pp. 549–560, 2023.
- [40] X.-S. Wu, X.-L. Dong, B.-Y. Wang, J.-L. Xia, and W.-C. Li, “Revealing the sodium storage behavior of biomass-derived hard carbon by using pure lignin and cellulose as model precursors,” *Renewable Energy*, vol. 189, pp. 630–638, 2022.
- [41] J. Wang, Y.-s. Li, P. Liu, F. Wang, Q.-r. Yao, Y.-j. Zou, H.-y. Zhou, M.-S. Balogun, and J.-q. Deng, “Green large-scale production of n/o-dual doping hard carbon derived from bagasse as high-performance anodes for sodium-ion batteries,” *Journal of Central South University*, vol. 28, no. 2, pp. 361–369, 2021.
- [42] E. Palmar, “Estructura poblacional de la palmera endémica *parajubaea torallyi* (mart.) burret en zonas aprovechadas del área natural de manejo integrado el palmar (chuquisaca, bolivia),” *Ecología en Bolivia*, vol. 44, p. 1, 2009.
- [43] M. R. Mónica and A. Henderson, “The genus *parajubaea* (palmae),” *Brittonia*, vol. 42, pp. 92–99, 1990.
- [44] F. Roca, “*Parajubaea cocoides*, a new record for peru.” *International Palm Society Inc*, 2010.
- [45] M. Moraes, “Novelties of the genera *parajubaea* and *syagrus* (palmae) from interandean valleys of bolivia,” *Novon*, pp. 85–92, 1996.
- [46] N. Abd Latif, N. Brosse, I. Ziegler-Devin, R. Chrusiel, Laurent, and H. M., “A comparison of alkaline and organosolv lignin extraction methods from coconut husks as an alternative material for green applications,” *BioResources*, vol. 17, no. 1, p. 469, 2022.

- [47] J. I. Goldstein, D. E. Newbury, J. R. Michael, N. W. Ritchie, J. H. J. Scott, and D. C. Joy, *Scanning electron microscopy and X-ray microanalysis*. Springer, 2017.
- [48] R. E. Lee, "Scanning electron microscopy and x-ray microanalysis," (*No Title*), 1993.
- [49] P. Echlin, C. Fiori, J. Goldstein, D. C. Joy, and D. E. Newbury, *Advanced scanning electron microscopy and X-ray microanalysis*. Springer Science & Business Media, 2013.
- [50] P. Larkin, *Infrared and Raman spectroscopy: principles and spectral interpretation*. Elsevier, 2017.
- [51] H. Kuzmany, *Solid-state spectroscopy: an introduction*. Springer Science & Business Media, 2009.
- [52] F. Wan, L. Du, W. Chen, P. Wang, J. Wang, and H. Shi, "A novel method to directly analyze dissolved acetic acid in transformer oil without extraction using raman spectroscopy," *Energies*, vol. 10, no. 7, p. 967, 2017.
- [53] S. Nandi, "Raman spectroscopy," 09 2021.
- [54] W. L. HOLLANDER, Jack M.; JOLLY, *X-ray photoelectron spectroscopy*. Accounts of chemical research, 1970.
- [55] C. Cushman, S. Chatterjee, G. Major, N. Smith, A. Roberts, and M. Linford, "Trends in advanced xps instrumentation. 1. overview of the technique, automation, high sensitivity, imaging, snapshot spectroscopy, gas cluster ion beams, and multiple analytical techniques on the instrument," *Vacuum Technology & Coating*, vol. 11, no. 01, 2016.
- [56] A. A. Bunaciu, E. G. UdriȘTioiu, and H. Y. Aboul-Enein, "X-ray diffraction: instrumentation and applications," *Critical reviews in analytical chemistry*, vol. 45, no. 4, pp. 289–299, 2015.
- [57] C. B. C. David B. Williams, *Transmission Electron Microscopy A Textbook for Materials Science*. Springer publication., 2009.

- [58] C. B. Carter and D. B. Williams, *Transmission electron microscopy: Diffraction, imaging, and spectrometry*. Springer, 2016.
- [59] G. N. Barrera, G. Calderón-Domínguez, J. Chanona-Pérez, G. F. Gutiérrez-López, A. E. León, and P. D. Ribotta, “Evaluation of the mechanical damage on wheat starch granules by sem, esem, afm and texture image analysis,” *Carbohydrate polymers*, vol. 98, no. 2, pp. 1449–1457, 2013.
- [60] A. B. Anderson and M. J. Balick, “Taxonomy of the babassu complex (orbignya spp.: Palmae),” *Systematic Botany*, pp. 32–50, 1988.
- [61] H. R. Amaral, D. F. Cipriano, M. S. Santos, M. A. Schettino Jr, J. V. Ferreti, C. S. Meirelles, V. S. Pereira, A. G. Cunha, F. G. Emmerich, and J. C. Freitas, “Production of high-purity cellulose, cellulose acetate and cellulose-silica composite from babassu coconut shells,” *Carbohydrate polymers*, vol. 210, pp. 127–134, 2019.
- [62] K. Thinkohkaew, N. Rodthongkum, and S. Ummartyotin, “Coconut husk (cocos nucifera) cellulose reinforced poly vinyl alcohol-based hydrogel composite with control-release behavior of methylene blue,” *Journal of Materials Research and Technology*, vol. 9, no. 3, pp. 6602–6611, 2020.
- [63] C. Chen, M. Wu, Y. Wang, and K. Zaghbi, “Insights into pseudographite-structured hard carbon with stabilized performance for high energy k-ion storage,” *Journal of Power Sources*, vol. 444, p. 227310, 2019.
- [64] A. Dilks and D. Clark, “Esca studies of natural weathering phenomena at selected polymer surfaces,” *Journal of Polymer Science: Polymer Chemistry Edition*, vol. 19, no. 11, pp. 2847–2860, 1981.
- [65] I. Childres, L. A. Jauregui, W. Park, H. Cao, Y. P. Chen *et al.*, “Raman spectroscopy of graphene and related materials,” *New developments in photon and materials research*, vol. 1, pp. 1–20, 2013.
- [66] R. Gond, H. D. Asfaw, O. Hosseinaei, K. Edstrom, R. Younesi, and A. J. Naylor, “A lignosulfonate binder for hard carbon anodes in sodium-ion batteries: a comparative

- study,” *ACS Sustainable Chemistry & Engineering*, vol. 9, no. 37, pp. 12 708–12 717, 2021.
- [67] J. Jehlička, O. Urban, and J. Pokorný, “Raman spectroscopy of carbon and solid bitumens in sedimentary and metamorphic rocks,” *Spectrochimica Acta Part A: Molecular and Biomolecular Spectroscopy*, vol. 59, no. 10, pp. 2341–2352, 2003.
- [68] G. Beamson, “High resolution xps of organic polymers. the scienta esca 300 database,” *ICIpIc*, 1992.
- [69] J. Wu, X. Du, Z. Yin, S. Xu, S. Xu, and Y. Zhang, “Preparation and characterization of cellulose nanofibrils from coconut coir fibers and their reinforcements in biodegradable composite films,” *Carbohydrate polymers*, vol. 211, pp. 49–56, 2019.
- [70] Q. Zhang, N. Bao, X. Wang, X. Hu, X. Miao, M. Chaker, and D. Ma, “Advanced fabrication of chemically bonded graphene/tio2 continuous fibers with enhanced broadband photocatalytic properties and involved mechanisms exploration,” *Scientific reports*, vol. 6, no. 1, p. 38066, 2016.
- [71] A. Shchukarev and D. Korolkov, “Xps study of group ia carbonates,” *Central European Journal of Chemistry*, vol. 2, pp. 347–362, 2004.
- [72] X. Chen, X. Wang, and D. Fang, “A review on c1s xps-spectra for some kinds of carbon materials,” *Fullerenes, Nanotubes and Carbon Nanostructures*, vol. 28, no. 12, pp. 1048–1058, 2020.
- [73] A. Ektessabi and S. Hakamata, “Xps study of ion beam modified polyimide films,” *Thin solid films*, vol. 377, pp. 621–625, 2000.
- [74] W. Lau, L. Huang, I. Bello, Y. Yiu, and S.-T. Lee, “Modification of surface band bending of diamond by low energy argon and carbon ion bombardment,” *Journal of applied physics*, vol. 75, no. 7, pp. 3385–3391, 1994.
- [75] T. G. Avval, S. Chatterjee, S. Bahr, P. Dietrich, M. Meyer, A. Thißen, and M. R. Linford, “Carbon dioxide gas, co2 (g), by near-ambient pressure xps,” *Surface Science Spectra*, vol. 26, no. 1, 2019.

- [76] B. Lesiak, L. Kövér, J. Tóth, J. Zemek, P. Jiricek, A. Kromka, and N. Rangam, “C sp²/sp³ hybridisations in carbon nanomaterials—xps and (x) aes study,” *Applied Surface Science*, vol. 452, pp. 223–231, 2018.
- [77] K. Harini and C. C. Mohan, “Isolation and characterization of micro and nanocrystalline cellulose fibers from the walnut shell, corncob and sugarcane bagasse,” *International Journal of Biological Macromolecules*, vol. 163, pp. 1375–1383, 2020.
- [78] Q. Wang, X. Zhu, Y. Liu, Y. Fang, X. Zhou, and J. Bao, “Rice husk-derived hard carbons as high-performance anode materials for sodium-ion batteries,” *Carbon*, vol. 127, pp. 658–666, 2018.
- [79] A. Gomez-Martin, J. Martinez-Fernandez, M. Rutttert, M. Winter, T. Placke, and J. Ramirez-Rico, “Correlation of structure and performance of hard carbons as anodes for sodium ion batteries,” *Chemistry of Materials*, vol. 31, no. 18, pp. 7288–7299, 2019.
- [80] L. Zhang, W. Wang, S. Lu, and Y. Xiang, “Carbon anode materials: a detailed comparison between na-ion and k-ion batteries,” *Advanced Energy Materials*, vol. 11, no. 11, p. 2003640, 2021.
- [81] Z. Wang, X. Feng, Y. Bai, H. Yang, R. Dong, X. Wang, H. Xu, Q. Wang, H. Li, H. Gao *et al.*, “Probing the energy storage mechanism of quasi-metallic na in hard carbon for sodium-ion batteries,” *Advanced Energy Materials*, vol. 11, no. 11, p. 2003854, 2021.